SIMULATION OF THE ION-BEAM-DRIVEN DRIFT INSTABILITY IN A MAGNETIC TRAP I

by

V. A. Thomas, W. M. Nevins, and Y-J. Chen

Memorandum No. UCB/ERL M84/45

13 June 1984

ELECTRONICS RESEARCH LABORATORY

College of Engineering
University of California, Berkeley
94720

Simulation of the Ion-Beam-Driven Drift Instability in a Magnetic Trap I.

V. A. Thomas

Electronics Research Laboratory, University of California,

Berkeley, CA 94720

W. M. Nevins and Y.-J. Chen

Lawrence Livermore National Laboratory, University of California,

Livermore, Ca 94550

ABSTRACT

Recent experiments on the TMX-U device at LLNL have indicated the possibility of a drift wave being driven unstable by the injection of neutral beams in the thermal barrier region. A review of linear theory is presented in the local approximation. In addition, particle simulations are used to understand the nonlinear characteristics of this instability. The particle simulations are performed using 1d - 3v and 2d - 3v electrostatic particle simulation codes. The instability is shown to saturate by beam trapping, nonlinear electron effects, and nonlinear motion parallel to the density gradient. Resonant $\mathbf{E}\times\mathbf{B}$ motion is a significant process for some of the beam particles. This process is closely asso-

ciated with the trapping of beam ions. Harmonic generation is also observed, as appears in some of the experimental data. Qualitative nonlinear theory is presented in support of the particle simulations.

June 9, 1984

Simulation of the Ion-Beam-Driven Drift Instability in a Magnetic Trap I.

V. A. Thomas

Electronics Research Laboratory, University of California,

Berkeley, CA 94720

W. M. Nevins and Y.-J. Chen

Lawrence Livermore National Laboratory, University of California,

Livermore, Ca 94550

1. Introduction

The theoretical study of collisionless drift waves was begun a number of years ago[1]. In particular, stability boundaries were given for the electrostatic electron drift wave in that original paper. The instability mechanism given in that paper was inverse Landau damping on the Maxwellian electron component. The Maxwellian ion component served to Landau damp the waves. The overall stability was then governed by the difference in the effects from the resonant electrons and resonant ions. Particle simulations have also been performed for this instability as in Ref. 2 and Ref. 3.

In this paper the analysis is extended to include the effects of injected ion beams as might occur in the thermal barrier cells of a tandem mirror device . For this case there is extra free energy associated with the ions which can cause instability . This ion-beam-driven drift

instability is a likely candidate for explaining some of the early experimental results on TMX-U at LLNL. It is in this context that the instability is of practical interest. This paper concentrates upon the instability for parameters similar to that of present day thermal barrier cells.

Section 2 reviews the linear theory using the electrostatic local approximation. Of particular interest is the dependence of growth rates and wavelengths on the relative density of the beam to the background plasma, the thermal spread of the beam along the magnetic field, and the zero order beam velocity perpendicular to the magnetic field.

Section 3 presents the simulation models and linear simulation results. Section 4 includes the qualitative nonlinear theory and the nonlinear results from the simulations. The characteristic nonlinear behavior includes nonlinear electron effects, mode coupling, ion beam trapping, and enhanced cross field motion of trapped beam ions. Section 5 includes a short discussion of the effects of axial inhomogeneity on the linear and nonlinear characteristics of the instability. A summary and conclusions are given in Section 6. Appendix A. presents a discussion of the field solves used in the particle simulation codes.

2. Linear Theory

In this section linear theory is examined in slab geometry using the local approximation. The effects of the various parameters of the problem are noted and the most unstable configurations are identified. Stabilizing effects are also presented.

A. Theoretical Model

The frequency regime of interest for this problem is $\omega << \Omega_{ci}$. In addition, it is assumed that $k_\perp \rho_e << 1$ and $\omega/k_z << v_{te}$. Only the electrostatic response is kept which is valid if the ion beam velocity U_b (along z) is much lower than the Alfven velocity. Variation of only the plasma density is considered and the magnetic field is assumed to be uniform in space. Under these conditions the dispersion relation may be written[4]

$$D(\mathbf{k},\omega,x) = \sum_s \chi_s = 0 \qquad (1)$$

where

$$\chi_s = -\frac{\omega_{ps}^2}{k^2}\int [\frac{\partial F_s}{\partial \epsilon_\perp} - \frac{GF_s J_0^2}{\omega - k_z v_z}] v_\perp dv_\perp dv_z \tag{2}$$

ω_{ps} is the unperturbed plasma frequency evaluated at a location x_0, $\epsilon_\perp \equiv (1/2)v_\perp^2$, $F_s(X,\epsilon_\perp,v_z)$ is the unperturbed guiding center distribution function with $X = x+v_y/\Omega_c$, the argument of the Bessel function is $k_\perp \rho_s$, and

$$G = \omega\frac{\partial}{\partial \epsilon_\perp} + k_z\left(\frac{\partial}{\partial v_z} - v_z\frac{\partial}{\partial \epsilon_\perp}\right) + \frac{k_y}{\Omega_c}\frac{\partial}{\partial X} \quad . \tag{3}$$

The plasma inhomogeneities are in the x direction which is perpendicular to the uniform magnetic field in the z direction. For consistency with the local approximation it is required that $(v_\perp/\Omega_c)\partial/(\partial X) << 1$ and that $k_y >> \partial/(\partial X)$.

For this parameter regime the electron response reduces to Debye shielding. The ion beam and background ion susceptibilities are more complicated. The distribution function for the beam or background ions may be taken as

$$F = (1 + \alpha[X - x_0])\frac{\delta(v_\perp - (v_\perp)_0)}{2\pi(v\perp)_0}\frac{1}{\sqrt{2\pi}v_{ti}}e^{-(v_z - v_0)^2/(2v_{ti}^2)} \tag{4}$$

where α is a constant, $v_{ti} \equiv \sqrt{(T_z/m_i)}$ being the ion parallel thermal speed, $v_0 = 0$ for the background ions and $v_0 = \pm U_b$ for the counter streaming beam ions. This model allows finite $k_\perp \rho_i$ effects and thermal effects. The model also makes it possible to consider the case where the zero order $v_\perp$ and v_z are comparable, which is a case of considerable practical interest.

For the moment, however, consideration will be given to the case where the ion beams and the background ions are completely cold and the beam ions have zero gyroradius. In this cold limit the physics is especially clear and the dispersion relation becomes

$$1 - \left(\frac{\delta}{2}\right)\frac{\omega_{pi}^2 k_z^2}{k^2}\left[\frac{1}{(k_z U_b - \omega)^2} - \frac{1}{(k_z U_b + \omega)^2}\right] - (1-\delta)\frac{\omega_{pi}^2 k_z^2}{k^2\omega^2} + \tag{5}$$
$$\left(\frac{\delta}{2}\right)\frac{\omega_{pi}^2 k_\perp \kappa_b}{\Omega_{ci} k^2}\left[\frac{1}{\omega - k_z U_b} + \frac{1}{\omega + k_z U_b}\right]$$
$$+\frac{\omega_{pi}^2 k_\perp^2}{k^2\Omega_{ci}^2} + (1-\delta)\frac{\omega_{pi}^2 k_\perp \kappa}{\Omega_{ci} k^2\omega} + \frac{1}{k^2\lambda_{De}^2} = 0$$

where δ is the ratio of the beam density to the total ion density, and

$$\kappa = \frac{1}{L_n} \equiv \frac{\frac{\partial n_{bg}}{\partial x}}{n_{bg}}\Big|_{x = x_0} \tag{6}$$

represents the inverse scale length of the background ion population evaluated at the location $x = x_0$ where the local approximation is being employed. ($\kappa_b = 1/L_b$ represents the inverse scale length in the ion beam density) The terms proportional to δ are from the ion beams. The terms with the frequency dependence of $1/\omega^2$ represent the parallel inertial response, the terms with the frequency dependence of $1/\omega$ represent the $\mathbf{E}\times\mathbf{B}$ response. The other ion derived term in the equation is from the polarization drift, which in this approximation of zero gyroradius is the same for both species of ions. Finally, only Debye shielding is retained for the electrons.

When δ is an infinitesimal quantity and the beam spatial gradients may be neglected the solutions to Eq. (5) are the drift wave branch

$$\omega^* = \frac{k_\perp \rho_s c_s \kappa}{1+k_\perp^2 \rho_s^2} \tag{7}$$

and the beam modes

$$\omega_{beam} = \pm\left|U_b \pm \sqrt{(\frac{\delta}{2})}c_s\right|k_z \quad . \tag{8}$$

Here c_s is the sound speed and $\rho_s \equiv c_s/\Omega_{ci}$. The solutions given in Eq. (7) and .Eq. (8) assume that the system is quasineutral. The solutions given in Eq. (7) and Eq. (8) are shown in Fig. 1. Notice that when $U_b > c_s$ and $U_b < c_s/(k_z 2L_n)$ the beam modes and the fast branch of the drift wave intersect, indicating that the the two modes are strongly coupled and instability may result. In Fig. 2. a numerical solution to the dispersion relation for a beam with finite density. Only the real portion of the frequency is plotted.

The approximate scaling for the parameters of this system can be obtained from Fig. 1. Specifically, $\omega_r = U_b k_z$, $k_\perp \rho_s = 1$, and $k_z L_n \leqslant c_s/(2U_b)$. The quasineutral approximation is good in the limit $\Omega_{ci} << \omega_{pi}$, which corresponds to the case of interest for thermal barrier cells. Note that the value for $k_\perp L_n$ remains unspecified. For consistency with the local approximation it is required that $k_\perp L_n >> 1$, which is valid in the limit $\omega << \Omega_{ci}$.

Note that the usual field-aligned electrostatic ion-ion two-stream instability is unstable under the opposite conditions in the cold limit; namely $U_b < c_s$. Since the drift wave is merely an extension of the sound wave for a situation where there is a density gradient, there is a close

connection between these instabilities. In some limits there will not be a unique way to name the instability since it may exist both with and without the density gradient.

B. Variation of Parameters

Variation of the characteristic parameters is expected to change the situation considerably from the cold limit. Some parameter variations are considered in this section. The most important of these parameters are the thermal spread of the ion beam parallel to the magnetic field , finite gyroradius effects, the beam fraction, the electron temperature, and the density gradients (which need not be the same for the different species). Attempting to vary all of the parameters is intractable and so only variation of one beam parameter at a time is considered. In addition, the background component is always assumed to be cold.

The plots of real and imaginary frequency will be scaled to the quantity $\omega_{max}^{\bullet} = .5c_s/L_n$, which frequency represents the maximum drift frequency for cold ions and vanishing k_z. It should be remembered however, that the analysis presented in this paper is valid only for $\omega << \Omega_{ci}$.

The general susceptibility for the ion beams including all of the parameters of the model is given by

$$\chi_i^{(b)} = \delta\left[\frac{\omega_{pi}^2}{\Omega_{ci}^2}\frac{K_\perp^2}{k^2} + \frac{\omega_{pi}^2}{k^2 v_{ti}^2}J^2{}_0(\xi)\left[1 + .5\sum_{\pm}\frac{\omega}{k_z\sqrt{2}v_{ti}}(1 \pm \frac{k_z U_b}{\omega} - \frac{\omega_i^{\bullet}}{\omega})Z(\frac{\omega \pm k_z U_b}{k_z\sqrt{2}v_{ti}})\right]\right] \quad (9)$$

where Z is the usual plasma dispersion function , $K_\perp^2 \equiv 2J_0(\xi)J_1(\xi)\xi\frac{\Omega_{ci}^2}{v_{\perp 0}^2}$, $\xi = \frac{k_\perp v_{\perp 0}}{\Omega_{ci}}$, and $\omega_i^{\bullet} = (k_\perp v_{ti}^2)/(\Omega_{ci}L_n)$. The set of parameters that are being used as a reference case are given in Fig. 2 and will be fixed unless otherwise noted.

Starting with a given set of parameters, it is desired to vary a given parameter and to follow the most unstable root. The equations that must be solved to find the most unstable root are

$$D(\omega,\mathbf{k}) = 0 \quad (10)$$

$$\mathrm{Im}\left[\frac{\partial D}{\partial \mathbf{k}}/\frac{\partial D}{\partial \omega}\right] = 0 \quad (11)$$

where k is taken to be a real quantity and the equations are solved for complex ω. The two equations given in Eq. (10) and Eq(11) constitute four nonlinear equations for the four unknowns $k_\perp$, k_z , the real part of the frequency ω_r and the growth rate γ. Efficient mathematical routines exist for solving such systems of equations[5]. These routines are used in a computer program written by one of us (Y.-J. Chen) and were very valuable in determining the behavior of the linear dispersion relation. Figures (3)-(7) were generated by this computer program.

One of the most striking effects is shown in Fig. 3, which demonstrates the effect of having the ion beam gradient not equal to the gradient of the background plasma. In particular, the growth rate is highest when the spatial gradients for the two species are in opposite directions. This is not a small effect. This effect is also possible to realize in experiments since the ion beam is created by external sources. For example when the optical depth of the neutral beam is short compared to the width of the system, the density gradients for the two ion species will be in opposite direction. In all of the following plots the ion beam gradient is set equal to zero so as to give an estimate of the more unstable situations which may occur. The qualitative effects of changing the other parameters are the same regardless of the value of the beam density gradient.

The effect of finite $k_\perp \rho_i$ for the beam ions is most clearly seen from the susceptibility given in Eq. (9). There it is seen that the destabilizing parallel drift terms are multiplied by $J_0^2(k_\perp \rho_i)$ and so as $k_\perp \rho_i$ becomes on the order of unity the effective beam density decreases. Since $v_{\perp_0}$ could be at least comparable to as U_b, the interesting values of $k_\perp \rho_i$ are could also be of order unity. A more complete description of finite gyroradius effects is given in Fig. 4 for a typical example. As the gyroradius of the beam ions is increased the growth rate decreases, the value of $k_\perp \rho_s$ decreases, and the real frequency also increases. All of these effects are consistent.

Variation of the beam parallel energy spread also reduces the growth rate of the most unstable mode. This is seen in Fig. 5. where the most unstable mode for a given case is

followed as the thermal spread is increased. The presence of resonant ions also forces the phase velocity of the wave along the field lines to decrease. The growth rate does not become negative, however. It is worth mentioning that the thermal spread is a slight destabilizing factor for one root which is otherwise stable.

In order to understand the electron effects more completely it is necessary to include the imaginary portion of the electron susceptibility. This is done by using

$$\chi_e = \frac{1}{k^2\lambda_{De}^2}\left[1 + \frac{(\omega - \omega_e^*)}{k_z\alpha_e} Z\left(\omega/(k_z\alpha_e)\right)\right] \tag{12}$$

where Z is the usual plasma dispersion function , $\alpha_e \equiv \sqrt{(2T_z/m_e)}$,and $\omega_e^* = -\frac{k_\perp T_e}{m_e \Omega_{ce}}\kappa_e$ with κ_e the inverse scale length of the electron population. Consider the addition of a small population of cool electrons For these electrons $\omega \geqslant \omega_{cool}^*$ and the most unstable mode is stabilized. Again as in the case of the ion thermal spread a mode which is stable with no cool electrons may made slightly unstable by the addition of the cool electrons.

Now consider the electrons consisting of a single hot species. Then $\omega \leqslant \omega_e^*$ and the most unstable mode is slightly destabilized. This effect is one effect which may cause the destabilization of drift waves with no free energy in the ion velocity space. The effect is, however, very small when $\omega/(k_z\alpha_e) << 1$ which corresponds to the cases of interest here. It should be noted that this discussion of the electron effects has assumed that the electron density gradient is in the same direction as that of the background ions. This assumption need not be true for the energetic electron component since their spatial distribution is greatly influenced by external factors (such as external heating). Therefore the electrons may serve to increase or decrease the growth rate of the most unstable mode, but in general cause only a small correction.

Figure 6 shows the effect of variation of the relative beam to background density. Notice that the maximum growth rate occurs for a value of δ less than one half. Also notice the other variables presented in Fig. 6. First of all , as the beam fraction approaches zero the real frequency approaches $U_b k_z$ as is expected. In this weak beam limit the growth rate γ is proportional to the square root of the beam density and the growth rate does not become zero (in the

cold limit) until the beam density itself becomes zero. In this weak beam limit the quantity $k_z L_n$ has its maximum value.

As the beam fraction increases the real frequency becomes lower for two reasons. First the beam modes begin to be split from the bounce frequency as in Fig. 2. Secondly, the maximum drift frequency propagating on the background plasma becomes smaller as the background density becomes smaller. Thus there would be no intersection of the beam modes with the drift wave branch unless the frequency of the beam mode was lowered. This is clearly seen in Fig. 6. where the real frequency, the growth rate and the value for $k_z L_n$ are all decreasing.

As the background beam density goes to zero, the interaction between the beam modes themselves needs to be considered since the beam modes may have some of the properties of the drift waves. When the background ion density does go to zero and the ion beams have their density gradients in the same direction (as in our case), no instability is present in any parameter regime.

Finally, the quantity U_b/c_s is allowed to vary and the results are shown in Fig. 7. The instability becomes more and more severe as the streaming velocity approaches the sound speed. As this happens the real frequency and k_z both increase very rapidly and the value for $k_\perp \rho_s$ goes to zero. In this limit the instability reduces to the field-aligned ion-ion two-stream instability[6,7] which has frequencies and growth rates on the order of ω_{pi} and the original approximation of keeping only the low frequency response is not valid. For those cases where the beam velocity is very close to the sound velocity the temperature of the beam and of the background become very important. Severe instabilities for cold beams may prove to be stable for more realistic distribution functions[7].

3. Simulation Model and Linear Results

This section describes the simulation techniques and the linear behavior of the instability as recovered from our particle simulations.

A. Simulation Model

The simulation geometry is presented in Fig. 8. The uniformity of the magnetic field is a consequence of the low beta approximation. As in Sec. 2, the electrostatic approximation is used and is valid if the beam velocity U_b is much less than the Alfven speed V_A. The simulation codes use nonlinear Boltzmann electrons and particle ions to solve Poissons equation (or quasineutrality) in the $y-z$ plane with a constant magnetic field in the z direction. The quasineutral approximation is valid in the limit $\omega_{pi}^2 >> \Omega_{ci}^2$, which is a realistic limit. The time step constraint is determined by stability of ion cyclotron waves. However, this does not mean that $\Omega_{ci}\Delta t << 1$ if only the particle guiding center motion is desired. The stability constraint due to the ion cyclotron waves can be removed by schemes using a biased, first order accurate time integration scheme[8], although this was not done for this paper. For the 1-d 3-v code only one direction is kept in the $y-z$ plane and periodic boundary conditions are used for both the particles and the fields. The boundary conditions applied to the fields for the 2-d 3-v code are periodic in the y direction and $E_n = 0$ at $z = 0$ and $z = L_z$. The particles are periodic in the y direction and specularly reflected in the z direction. Therefore this 2-d 3-v simulation model is a type of square - well model for the thermal barrier region. Only those Fourier modes which are important for the instability are kept self-consistently in the codes.

The density variation is in the x direction and is implemented using the " ghost particle " technique from Cohen[9]. The ghost particle technique assumes a fixed density profile for the various species and has the drawback that the density profile cannot be self-consistently updated. Thus, final saturation levels from the simulations can be expected to retain only qualitative information. This ghost particle technique is useful when velocity-space relaxation may saturate the instability, as for the instability being studied in this paper. The exact form of the density variation may be specified arbitrarily. For our simulations we have found it convenient to use $n(x) = n_0(1 + rx/(1+|rx|))$ where $rx = x/L_n$ is the displacement relative to the local density scale length. In order to restrict the parameter space, the beam scale length was taken to be infinite, which represents the more unstable possibilities as seen in Fig. 3. Since the ions must have a x coordinate associated with them, the 2-d 3-v code has six phase space variables

and the 1-d 3-v code has five phase space variables.

B. Linear Simulation Results

In this section representative linear code behavior is presented. Excellent agreement with theory is obtained for the simplified distribution functions used in the simulations.

Initially we consider the case of parallel injection only; that is $v_\perp = 0$. A series of test runs was conducted in order to compare the theoretical growth rates and those given by the 2-d 3-v simulation code. The simulations parameters were $\delta = 0.2$, $U_b/c_s = 3.0$, $\Omega_{ci}\Delta t = 0.5 - 1.0$, $\omega_{max}/\Omega_{ci} = .03$ and only one Fourier mode was kept. The normalized parallel drift velocity, $v_{\parallel}/U_b$, was varied and the system lengths were changed so that the most unstable mode was retained. There were $N_y = 65$ grid cells in the y direction and $N_z = 32$ grid cells in the z direction. Approximately 25,000 particles were used. For these parameters the $k_\perp L_n \geqslant 10$ and the local approximation can be expected to retain some validity, at least in the linear regime. The parallel velocities were chosen by bit-reversing technique as in Birdsall and Langdon[10]. This allowed much cleaner results than from a random initialization.

An example is given in Fig. 9 of the square of the mode amplitude as a function of time. Note that the line is not perfect. This is to be expected since for this simulation resonant particles play a large role in the determination of the growth rate. Also, the simulation could be started without initial excitation in which case the total growth in field amplitude would be about double what it is here. The characteristics of the results are the same when this is done. Finally, the five test cases are given in Fig. 10 along with the calculated growth rates from Sec. 2. The boundary conditions used by the 2-d 3-v code do not change the growth rate from infinite medium theory. Agreement is very good. The error is on the order of the error made in the theoretical treatment; that is the error is on the order of ω/Ω_{ci}.

The injection angle of the neutral beams relative to the magnetic field in the thermal barrier cell is designed to be approximately forty five degrees[11]. Therefore the zero order $v_\perp$ should be approximately equal to the zero order streaming motion along the magnetic field. This can be and has been added to the simulation model. However the additional noise associated with

the ion cyclotron waves requires a very large number of particles to suppress. Thus the particle simulations become prohibitively expensive. One could try to use a guiding center mover[12] or a gyrokinetic approach[13] in order to eliminate ion cyclotron modes and still retain finite gyroradius effects. However, because the instability characteristics are insensitive to finite gyroradius, finite gyroradius effects will be ignored for numerical efficacy. Specifically, the linear characteristics are insensitive to finite $k_\perp \rho_i$ corresponding to the most unstable mode. Similarly, quasilinear effects are only modified by a multiplicative factor $J_0^2(k_\perp \rho_i)$ from the case with zero gyroradius[4].

4. Nonlinear Behavior

This section describes the nonlinear phenomena as observed from the simulations and presents a qualitative discussion of their importance. The nonlinear phenomena include (1) nonlinear electron effects , (2) nonlinear motion in the density gradient direction, (3) mode coupling, and (4) trapping of the beam ions. The relative importance of these effects depends upon the (1) the linear growth rate , (2) the parallel thermal spread in the ion beams and (3) the relative density of the ion beams to the background plasma.

A. Motion in a Single Wave

The unstable modes that are present have their phase velocities lower in absolute values than the beam velocity as seen in Fig. (2). The qualitative condition for trapping depends upon whether the ion beam is warm or cold. Here the beam would be labeled as warm if many beam particles were resonant with the parallel phase velocity of the unstable wave. If the beam is thermal in that sense, then saturation could be due to the nonlinearities associated with resonant particles. If this happens, then saturation occurs within about an e-folding time of when the growth rate is equal to the bounce frequency of the resonant particles in the wave. Estimation of the perturbed potential at saturation by this method yields the scaling law

$$\frac{e\delta\phi}{T_e} \approx \frac{\gamma^2\alpha^2}{\omega_b^2}3 \tag{13}$$

where $U_b = \alpha c_s$ and $\omega_b \equiv k_z U_b$ and the factor 3 represents the " e-folding " of the amplitude

after the onset of nonlinear behavior. Typically this predicts values for $(e\delta\phi)/T_e \leqslant 1$ which restricts the choice for the electron model. In particular, a linearized electron response cannot always be expected to yield correct results.

However, if the beam fraction is large enough and the beam temperature is low enough so that the phase velocity lies substantially outside the ion distribution function, then the perturbed saturation potential at saturation must be larger than predicted by Eq. (13). It is for these cases of a cold and strong beam that ion trapping is not the only significant saturation mechanism. The nonlinear electron response and displacements of the background ions of $x/L_n \leqslant 1$ play major roles in limiting the perturbed potential. Under these conditions where the background displacement becomes nonlinear, the local approximation becomes more tenuous. A more complete nonlocal treatment will be considered separately in a later publication.

Closely associated with particle trapping in a single wave is an enhanced cross-field motion of the particle guiding center parallel to the equilibrium density gradient. As shown by Nevins[14] this guiding center constant may be expressed as

$$v_z - \left(k_z/k_y\right)\Omega_{ci}x = constant \tag{14}$$

where the field has the form $\phi = \phi_0(x)\sin(k_y y + k_z z - \omega t)$. Therefore large changes in v_z are accompanied by large excursions parallel to the equilibrium density gradient. This effect is most prominent for resonant particles since resonant particles suffer the largest changes in v_z.

The electrostatic field is polarized almost perpendicular to the magnetic field and so it is natural to consider the possibility that the instability may be saturated by perpendicular trapping, that is that the perturbed electric force should be comparable to the magnetic force. Setting those two forces equal gives

$$\frac{e\delta\phi}{T_e} \approx \frac{\alpha^2\Omega_{ci}^2}{U_b^2 k_\perp^2} \tag{15}$$

Comparing Eq. (13) and Eq. (15) suggests that perpendicular trapping should dominate over parallel trapping when

$$\frac{\Omega_{ci}^2}{\gamma^2} \leqslant \frac{k_\perp^2}{k_z^2} \tag{16}$$

is satisfied. This condition is very difficult to satisfy as $k_\perp \rho_s \approx 1$ and $\gamma \leqslant 0.1 k_z U_b$ make it possible to rewrite Eq(15) as

$$\frac{U_b}{c_s} \geqslant 100 \quad . \tag{17}$$

B. Motion with Several Waves

The presence of several waves complicates the analysis. First of all, even for a single value of $k_\perp$ there exist two unstable waves. One wave has positive phase velocity along the magnetic field (positive k_z) and the other wave has negative phase velocity (negative k_z) along the magnetic field. The wave with positive phase velocity is associated with instability in the beam with positive velocity and similarly the wave with negative phase velocity is associated with instability in the beam with negative velocity.

However, the presence of two waves (one with a negative phase velocity along the magnetic field and the othe with a positive phase velocity along the magnetic field) causes no significant change over the case of a single wave. The reason is that in the frame of one of the beams, the two phase velocities of the unstable waves are vastly different. The wave in approximate resonance with a given beam is responsible for nonadiabatic change of that beam. The other wave is of very high frequency and only causes high frequency adiabatic motion of the particles in that beam.

Next, we consider the case of multiple values of **k**. Frequently, it is claimed that multiple waves lead to quasilinear diffusion. However, this is subject to two constraints; (1) that the wave autocorrelation time is short compared to the trapping frequency and (2) that the number of unstable waves present is large. Both of these requirements may not be met for experimental or for the simulations. One reason for this is that all of the unstable waves have parallel phase velocities of $\approx \pm U_b$ as seen in Fig. 11. Thus the wave autocorrelation time is very long. In addition both in experiment and in simulation the **k** spectrum is discrete. The discrete nature of the **k** spectrum is an important consideration in most simulations. Typically, in a simulation, a single mode dominates the saturation process.

A more complete treatment would have to include both axial and radial inhomogeneities. These two effects may alter the picture given in the preceding paragraph using the infinite medium model. The complete radial problem is a boundary value problem and as such may have a number of unstable eigenfrequencies for a given value of k_y and k_z. In particular, for those cases where the local approximation is satisfied the eigenfrequencies are closely spaced. Thus the complete radial problem may have many more waves with comparable growth rates than local analysis yields. This fact should tend to increase quasilinear effects.

Axial inhomogeneities change the problem by causing the normal modes to be composed of many values for k_z rather than one value as for the homogeneous case. Thus, axial variation of equilibrium parameters may assist is making quasilinear diffusion a more important mechanism than predicted by infinite medium theory.

C. Weak Mode Coupling

Experimentally it was seen that for weak cold beams there were peaks in the spectrum of the noise at harmonics of the ion bounce frequency in the magnetic well. The number of harmonics seen was much larger than the likely number of unstable modes. This implies a possible mode coupling mechanism.

The theoretical treatment is outlined below. The treatment of Sagdeev and Galeev[4] is followed. The particle distribution function is expanded in a series in the small parameter η as

$$f = \sum_{s=0}^{\infty} f^{(s)} \eta^s \tag{18}$$

and

$$\phi = \sum_{s=0}^{\infty} \phi^{(s)} \eta^s \tag{19}$$

The series for the distribution function may be calculated by using

$$\delta f^{(s)} = \eta \int_{-\infty}^{t} dt' \nabla \phi \cdot \frac{\partial f^{(s-1)}}{\partial \mathbf{v}} \tag{20}$$

where the integration is over the unperturbed particle trajectory. Poisson's equation then closes the system of equations for each order in η.

The equation giving the second order behavior for a mode $(\mathbf{k},\omega)$ which is linearly stable is given by

$$\phi^{(2)}\left(\mathbf{k},\omega\right) = -\sum \frac{\epsilon^{(2)}\left(\mathbf{k}',\mathbf{k}'',\omega'\omega''\right)}{\epsilon^{(1)}(\mathbf{k},\omega)} \phi_{\mathbf{k}'}^{(1)} \phi_{\mathbf{k}''}^{(1)} \tag{21}$$

where the sum is over all modes which satisfy the conditions $\mathbf{k}' + \mathbf{k}'' = \mathbf{k}$ and $\omega' + \omega'' = \omega$. This expression contains a very complicated function $\epsilon^{(2)}$ and the linear response given by $\epsilon^{(1)}$. Equation (21) actually assumes that modes $(\mathbf{k}',\omega')$ and $(\mathbf{k}'',\omega'')$ are marginally stable. However, it does represent the correct first order expansion in γ/ω and so retains qualitative justification even for finite growth rate. One relevant fact is that the linear response may become small. This is realistic if both the beam density and the beam thermal spread are both small. Under these conditions harmonic generation is possible.

D. Simulation Results in the Nonlinear Regime

As indicated above, there exist several nonlinear mechanisms associated with the saturation of the instability. These nonlinear effects will be demonstrated be using the results for the one dimensional code and the two dimensional code. In addition to the saturation mechanisms, the appearance of ion phase space at saturation is important and therefore will be described.

The 1-d 3-v model allows only one of the beams to be unstable since only one sign of k_z relative to $k_\perp$ is allowed. Nevertheless, this model is a useful starting point for examining nonlinear effects. For example Fig. 12 shows particle trapping and enhanced cross field motion near saturation of the instability. The existence of the guiding center constant of motion dictates the symmetry seen in the two plots. This simulation was of a cold strong ($\delta = 0.2$) beam with the parameters of Sec. 3B. and as a result nonlinear electron effects and nonlinear motion of the background ions ($x/L_n \leqslant 1$) were also important factors in saturation of the instability.

A more complete model of the instability is obtained with the 2-d 3-v simulation code, since for this code both beams are unstable in the simulation. This code was used to generate a series of simulations with varying thermal spread. The thermal spread plays a large role in determining the magnitude of $(e\delta\phi/T_e)$, at saturation and the appearance of $f(v_z)$ at satura-

tion.

The simulation parameters are the same as used in Sec. 3B. Table 1 gives the amplitude of the perturbed potential at field energy saturation. Notice that the Boltzmann electron response is important since $e\delta\phi/T_e$ is not neccesarrily a small parameter. Simulations were performed using a linearized electron response and the saturation levels for the cold beam cases were significantly (and unphysically) enhanced.

The distribution function at saturation is also useful for demonstration of nonlinear effects. These distribution functions are given in Fig. 13. For the cooler cases the entire beams become nonlinear and resonant particle trapping is not seen. As the beam thermal spread becomes larger and larger, obvious trapping effects are seen. This trapping is confined to the resonant particles and the bulk of the distribution function remains linear as shown in Fig. 14.

Finally, several multimode simulations were studied to examine the effects of retaining additional stable and unstable wavevectors. Keeping additional unstable wavevectors caused only slight differences in the single mode cases mentioned above. This is due to the discrete nature of the simulation **k** space; only a small number of modes have comparable growth rates. For example, Fig. 15 shows the dominant nonlinear behavior for a simulation in which many modes were linearly unstable. As can be seen (Fig. 15) the constant of motion given in Eq. (14) is still very useful.

Keeping additional stable wavevectors at multiples of the unstable wavevectors does lead to mode coupling. This effect is most prominent for weak cold beams as mentioned in Section 4B. One example is given in Fig. 16. The extent of coupling obtained in this matter can not be compared quantitatively to the experiments, since the experimental results depend on many more parameters than included here.

The nonlinear effects are summarized in Table 2. For the case most relevant to experimental operation, that of a strong thermal beam, the saturation is by beam trapping and weakly nonlinear electrons. For beams with very large thermal spreads parallel to the magnetic field, the growth rate becomes very small and the electrons remain linear.

5. Axially Inhomogeneous Simulations

This section is a preliminary study of the effects of axial inhomogeneity on both the linear and nonlinear evolution of the instability. It is shown that considerable shortening of the axial length is necessary for significant decrease of the field amplitude at saturation.

In order to relax the square well approximation of the previous section an axially non-uniform electron response was used. The model electron response is given by

$$n_e(z) = n_0 \exp\left[e\phi/T_{\|e}(z)\right] \tag{22}$$

where the function $T_{\|e}(z)$ represents the parallel electron temperature and is a function chosen to model the thermal barrier cell. The most important feature that the model must retain is that the effective electron temperature increases toward the middle of the thermal barrier cell.

The model used is not entirely self-consistent because the magnetic field is assumed to be axially uniform for pushing the ions. In reality, the reason for the effective electron temperature to vary axially is that energetic electrons are trapped in an axial magnetic well. The effect of the axially varying magnetic field can be neglected for the ions in the center of the magnetic well if the mirror ratio is large and the ions are injected near the mirror throat. The ion motion in the stable regions then just gives a time delay and the details of that motion are irrelevant.

This approach makes it possible to examine qualitatively new physics as compared to the square well model. Unstable regions are now limited to the region in the center of the cell where the instability condition $U_b k_z \approx c_s/(2L_n)$ can be satisfied. Further away from the well center c_s is much smaller and unstable values of k_z are not able to fit into the system. A complete theoretical treatment of the problem must include all of the bounce resonances in the well as in Sharp[15]. This will not be attempted in this paper.

In order to perform simulations a choice must be made for the function $T_{\|e}(z)$. Several different functions were tried; the qualitative effects were found to be independent of the exact functional form employed. For the simulations presented here the functional form was chosen (1) to be symmetric about the center of the simulation region, (2) to be constant near the edges of the simulation region, (3) to be parabolically increasing near the center of the

simulation region, and (4) to be a continuous function. The simulations used $N_z = 65$ with the parabolic region confined to the girds larger than grid number 8 and smaller than grid number 57. The other simulation parameters were $N_y = 32$, $\delta = 0.2$ $\omega^*_{max}/\Omega_{ci} = 0.03$, $v_{ti}/U_b = 0.13$ and $U_b/c_s = 3.0$ where c_s is evaluated at the center of the simulation region. Only one Fourier mode was kept in the y direction. Approximately 25,000 particles were used. The system length was varied.

Figure 17 shows the effect of axial inhomogeneity on a typical potential profile. (case 2 of Table 3.) The perturbed potential is substantially limited to the center of the simulation region where the electron Debye shielding is the weakest. However, the potential need not be symmetric about the simulation midplane even though the electron response is symmetric. Also, the general case will have more than one normal mode present at the same time if the excitation is random as in the simulation presented here. This is seen to be the case from Fig. 18 where a time history of the real part of the potential is given for a location near the center of the system.

The saturation of the instability is very similar to that of the square well simulations. This can be seen from the test particle trajectories presented in Fig. 19. Again the qualitative behavior is similar to that dictated by the adiabatic constant of motion. Table 3 shows the values of the perturbed potential at saturation as the system length is varied. Notice that a dramatic decrease is not attained except when the most unstable wavelength is longer than about twice the length of the unstable region.

6. Conclusions

In this paper a simulation model has been used to examine a drift wave instability which has been observed in some experiments. Qualitative nonlinear behavior demonstrates the importance of beam trapping, cross-field diffusion, and nonlinear electron effects. In addition the importance of the thermal spread in determining the saturation behavior has been shown.

Acknowledgements

The authors appreciate useful discussions with Professor C. K. Birdsall, Dr. Jack Byers, Dr. T. A. Casper, Dr. Bruce Cohen and Dr. Tom Crystal.

This research was partially supported by the Office of Naval Research Contract No. N00014-77-c-0678 (Berkeley), and in part by the Department of Energy under Contract No. DE-AM03-76SF00034 (Berkeley). The computations were performed at the National Magnetic Fusion Energy Computer Center at Lawrence Livermore National Laboratory.

Appendix A.

The electrostatic field solver used in the simulations is described in this appendix. The field solve uses either (a) linear electron Debye shielding in conjunction with Poisson's equation (b) quasineutral Boltzmann electrons or (c) Boltzmann electrons in conjunction with Poisson's equation. For the parameters of the paper, the second option was quite adequate.

The field solve using completely nonlinear Boltzmann electrons is solved for in a manner using techniques given in Hockney and Eastwood[16]. Given an initial approximation to Poisson's equation ϕ^p, Poisson's equation is linearized with respect to that approximate solution yielding

$$\nabla^2\phi^{p+1} = en_0\exp\frac{e\phi^p}{T_e}\left[1 + \frac{e(\phi^{p+1} - \phi^p)}{T_e}\right] - en_i \tag{A1}$$

where ϕ^{p+1} is the next approximation for the potential. Subtracting $\nabla^2\phi_p$ from both sides of the equation yields an equation for the small quantity $W \equiv \phi^{p+1}-\phi^p$ given by

$$\nabla^2 W = -en_i - \nabla^2\phi^p + en_0\exp\left[\frac{e\phi^p}{T_e}\right] + Wen_0\exp\left[\frac{e\phi^p}{T_e}\right] \tag{A2}$$

To solve this equation the iterative method of Concus and Golub[17] is used. This consists of removing (approximately) the W depend of the right hand side of Eq. (A2). This yields

$$\left[\nabla^2 - K\right]W^{n+1} = \left[-en_i - \nabla^2\phi^p - KW^n\right] + \frac{e^2}{T_e}W^n n_0\exp\left[\frac{e\phi^p}{T_e}\right] + en_0\exp\left[\frac{e\phi^p}{T_e}\right] \tag{A3}$$

Here K is a parameter which may be varied to improve convergence. The optimum value is that value which approximately removes the W dependence of the rhs. Given the updated potential, the entire procedure is started again.

References

1. N. A. Krall and M. N. Rosenbluth, Phys. Fluids **8** , 1488 (1965).
2. W. W. Lee and H. Okuda, Phys. Rev. Lett. **36**, 870 (1976).
3. C. Z. Cheng and H Okuda, Phys. Rev. Lett. **38**, 708 (1977).
4. R. Z. Sagdeev and A. A. Galeev, *Nonlinear Plasma Theory* , Benjamin, New York (1969).
5. Numerical Algorithms Group, Inc., 1131 Warren Ave., Downers Grove Illinois 60515.
6. E. A. Foote and R. M. Kulsrud, Phys. Fluids **24** , 1532 (1981).
7. V. A. Thomas and W. M. Nevins , Submitted For Publication.
8. D. C. Barnes, T. Kamimura, J.-N. Leboeuf, and T. Tajima, J. Comp. Physics, **52** , 480 (1983).
9. B. I. Cohen, N. Maron, and G. R. Smith, Phys. Fluids **25** , 821 (1982).
10. C. K. Birdsall and A. B. Langdon, *Plasma Physics Via Computer Simulation*, McGraw-Hill, New York (1984).
11. T. J. Orzechowski, S. L. Allen, J. H. Foote, R. K. Goodman, A. W. Molvik, and T. C. Simonen, Phys. Fluids **26** , (1983).
12. W. W. Lee and H. Okuda, J. Comp. Phys. **26** , 139 (1978).
13. W. W. Lee, Phys. Fluids **26** , 556 (1983).
14. W. M. Nevins, Phys. Fluids **22** , 1667 (1979).
15. W. M. Sharp, H. L. Berk and C. E. Nielsen, Phys. Fluids **22** , 1975 (1979).
16. R. W. Hockney and J. W. Eastwood, *Computer Simulation Using Particles* , McGraw-Hill (1981).
17. P. Concus and G. H. Golub, SIAM J. Numer. Anal. **10** , 1103 (1973).

Saturation Dependence of Thermal Spread					
v_{ti}/U_b	0.01	0.07	0.13	0.19	0.25
$\gamma_{max}/\omega^*_{max}$	0.13	0.12	0.095	0.073	0.052
$(e\delta\phi/T_e)_{sat.}$	0.35	0.33	0.29	0.22	0.15

TABLE 1. Variation of saturation with the parallel thermal spread of the ion beams. For larger thermal spreads the saturation levels should decrease very quickly since for those cases trapping is the sole saturation mechanism.

Saturation Characteristics		
δ	v_{ti}/U_b	
	small	large
weak	ion beam trapping; enhanced cross-field motion of trapped ions; coherent mode coupling	trapping of resonant ions; enhanced cross-field motion of trapped ions
strong	nonlinear electrons; non-linear motion parallel to the density gradient; ion beam trapping; enhanced cross field motion of trapped beam ions	trapping of resonant ions; enhanced cross-field motion of trapped ions; weakly non-linear electrons

TABLE 2. Nonlinear properties as a function of parameter space.

Saturation Levels as a Function of System Length	
ψ	$(e\delta\phi/T_e)_{saturation}$
10.0	0.38
5.0	0.37
2.5	0.15

TABLE 3. Saturation levels as a function of system length. The parameter ψ is the system length divided by half of the most unstable wavelength evaluated locally at the center of the system. The parameter T_e represents the electron temperature in the center of the simulation region.

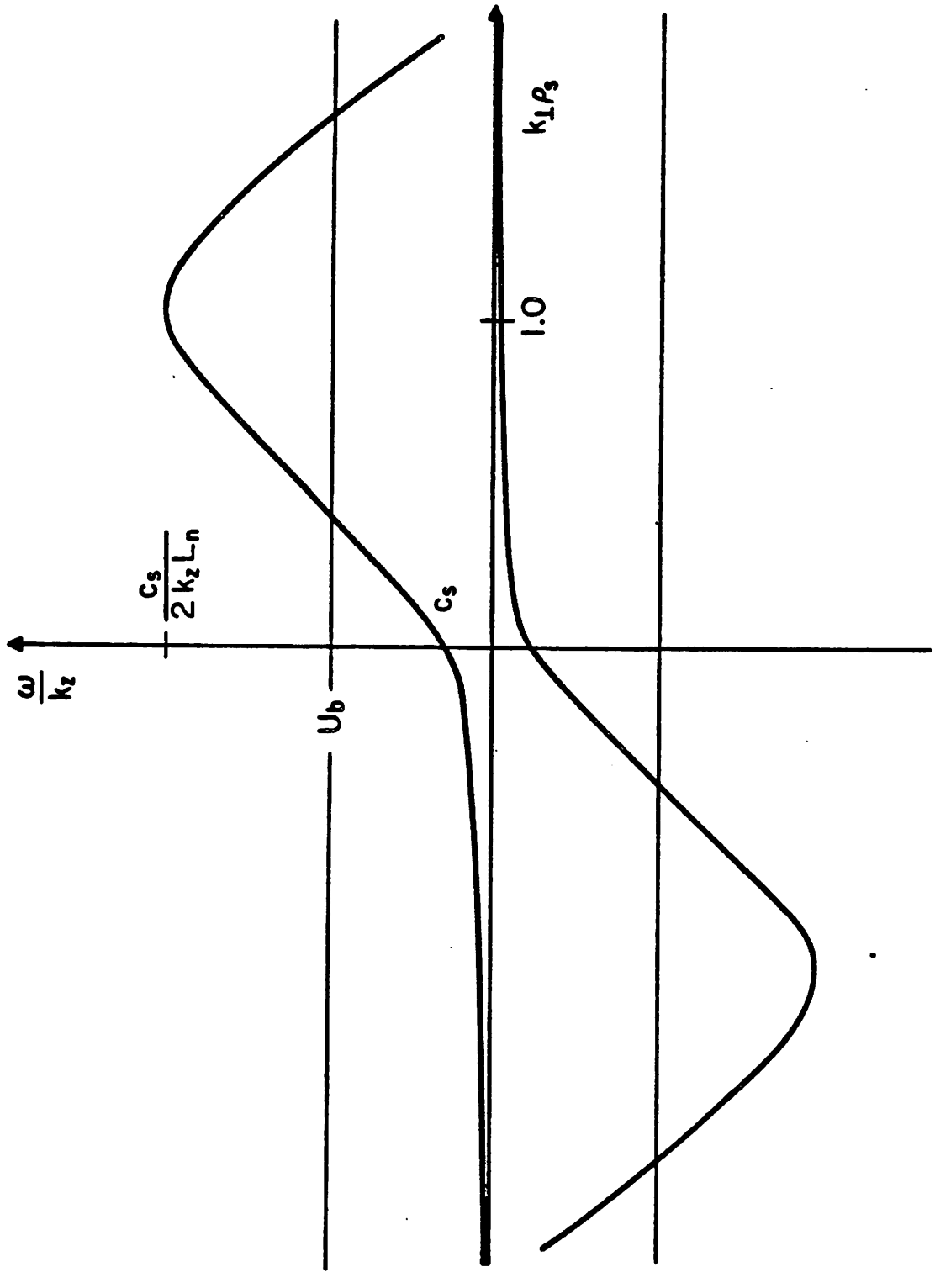

FIG. 1. Schematic solutions to the dispersion relation in the weak beam limit.

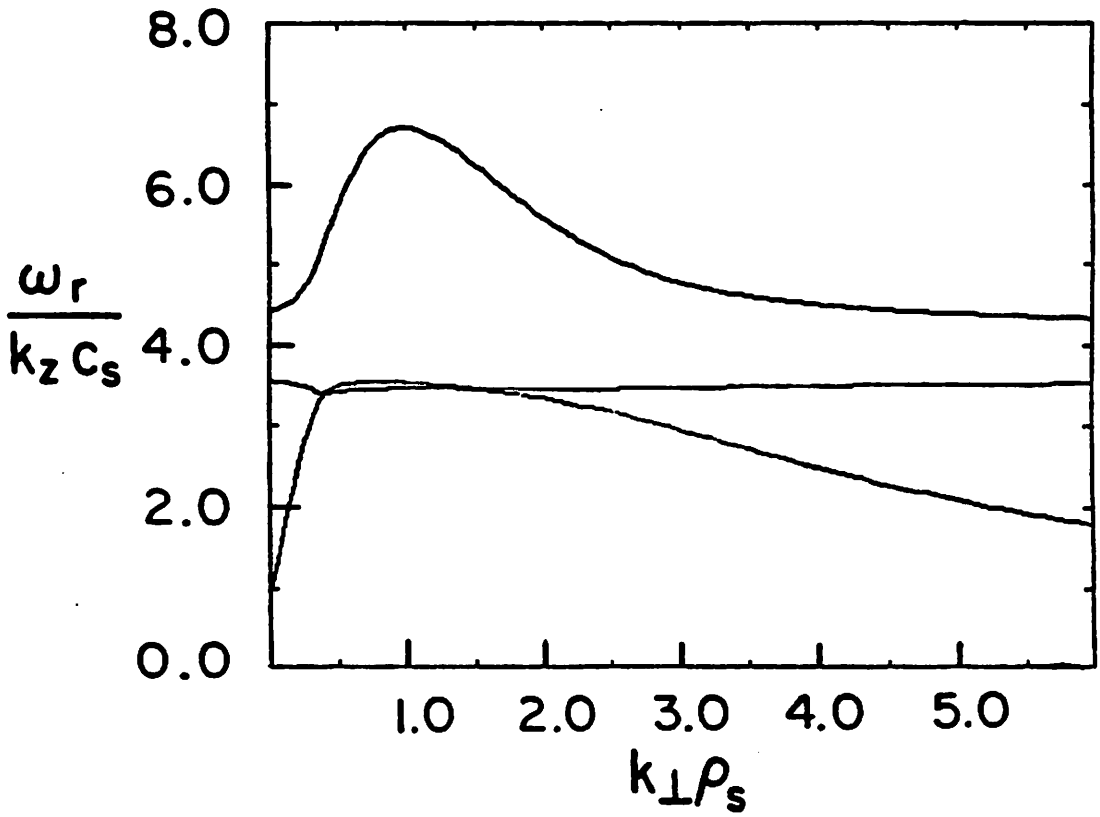

FIG. 2. Real frequencies for a numerical solution for a typical set of parameters; $\delta = .1$, $U_b/c_s = 4.0$, $v_{ii}/U_b = 0.05$, $v_\perp/U_b = 0.0$, and $k_z L_n = .1$. The peak in the growth rate occurs just after the intersection of the real frequencies.

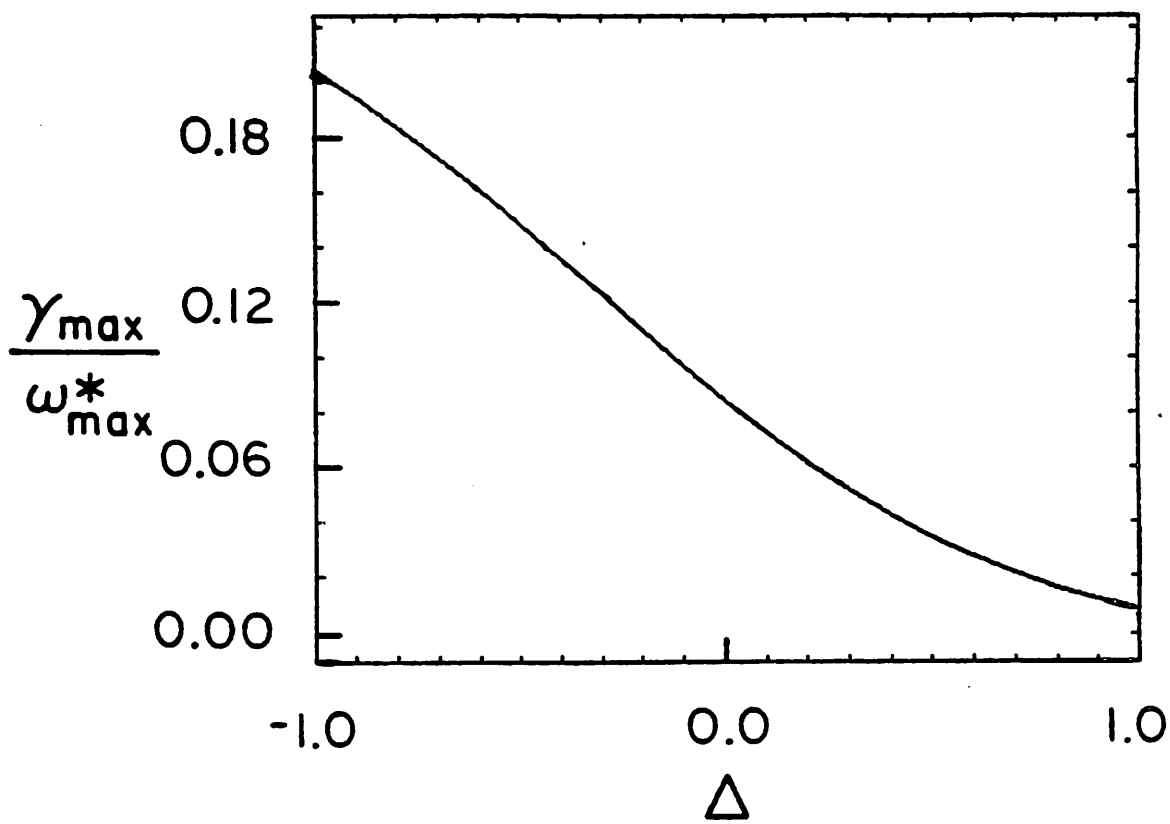

FIG. 3. (a) Normalized maximized growth rate $\gamma_{max}/\omega^{\cdot}_{max}$ maximized over the **k** vector as a function of $\Delta \equiv L_n/L_b$ and the corresponding values of (b) the normalized real frequency $\omega_r/\omega^{\cdot}_{max}$, (c) $k_{\perp}\rho_s$, and (d) $k_{\parallel}L_n$. The scale length of the background plasma, L_n, is held fixed while the scale length of the beam, L_b is varied.

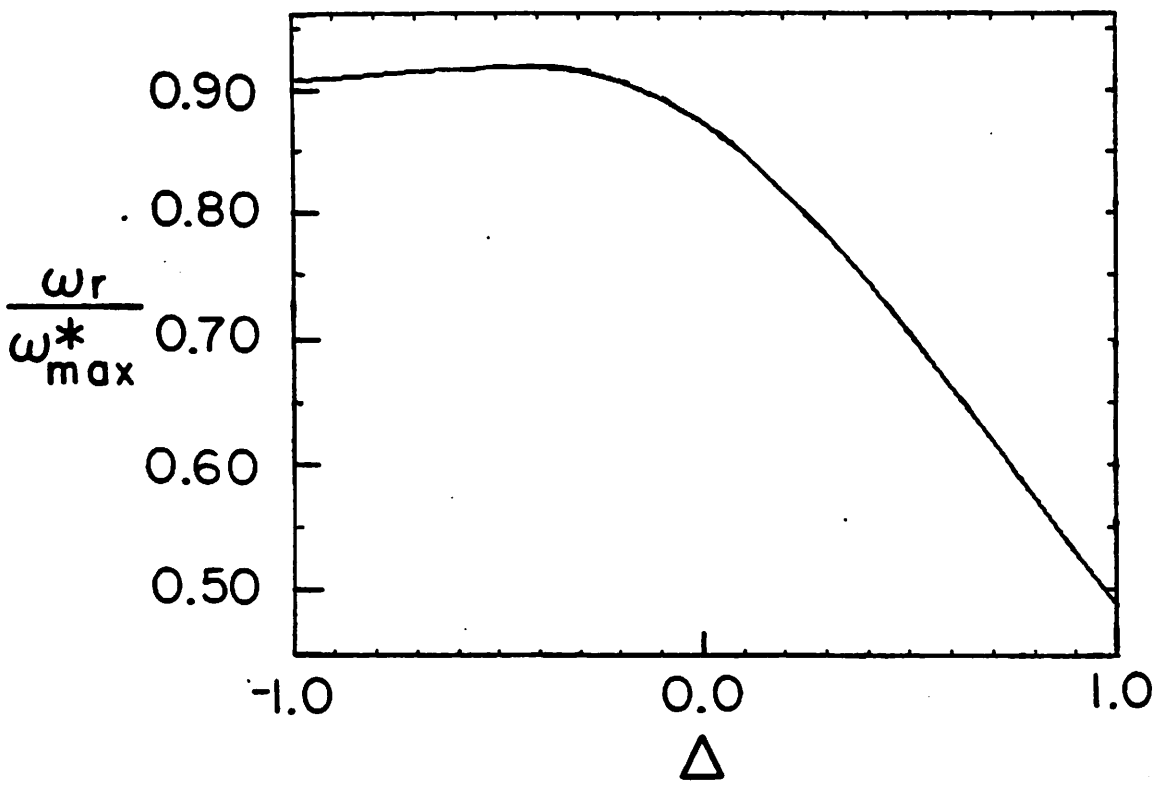

FIG. 3b.

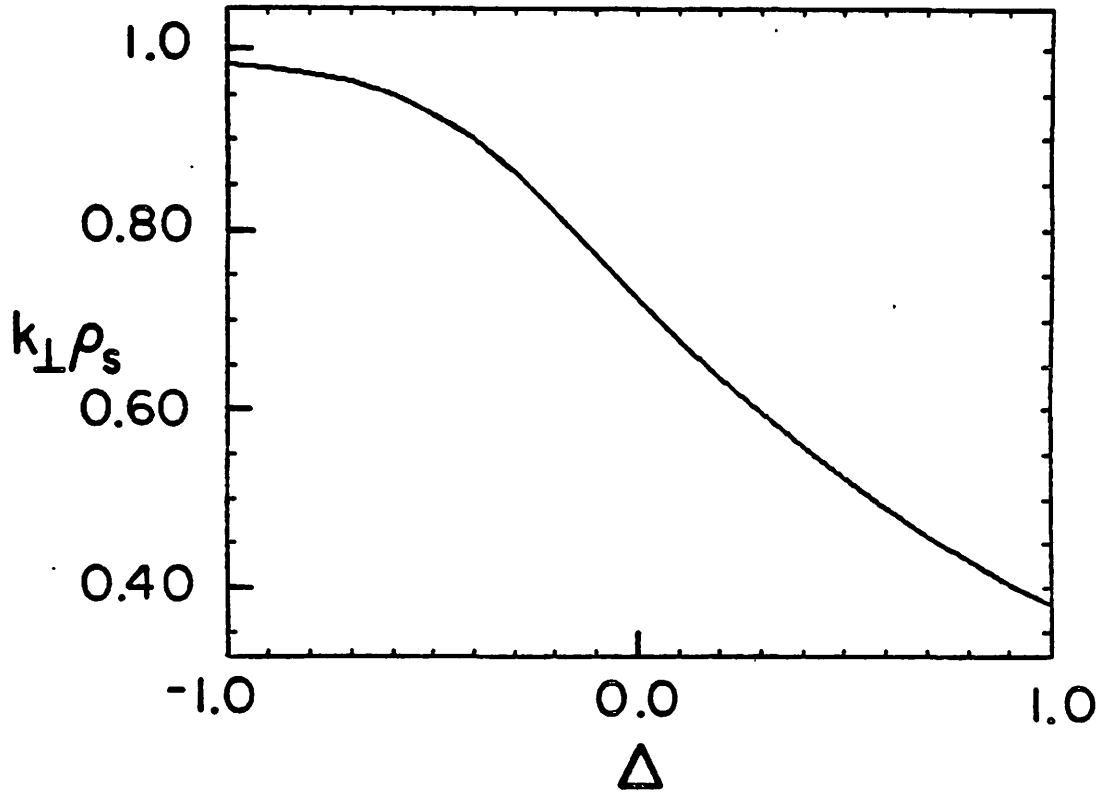

FIG. 3c.

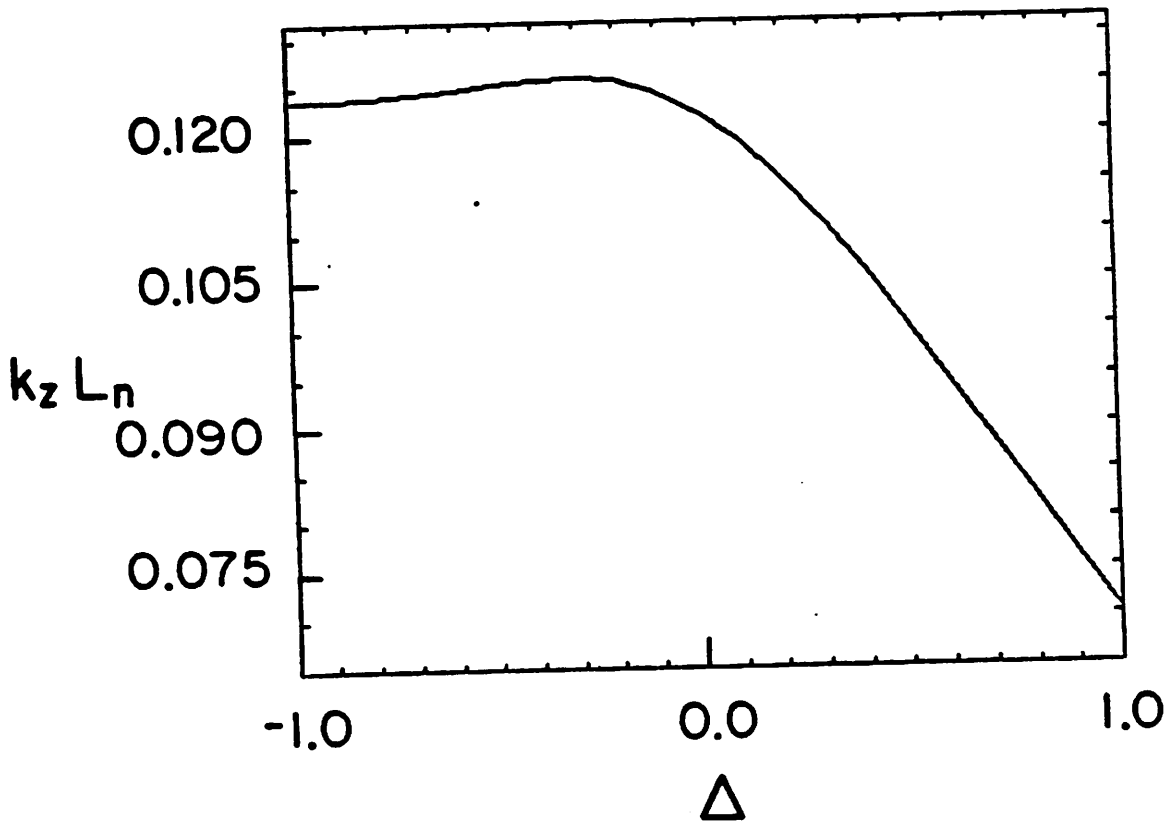

FIG. 3d.

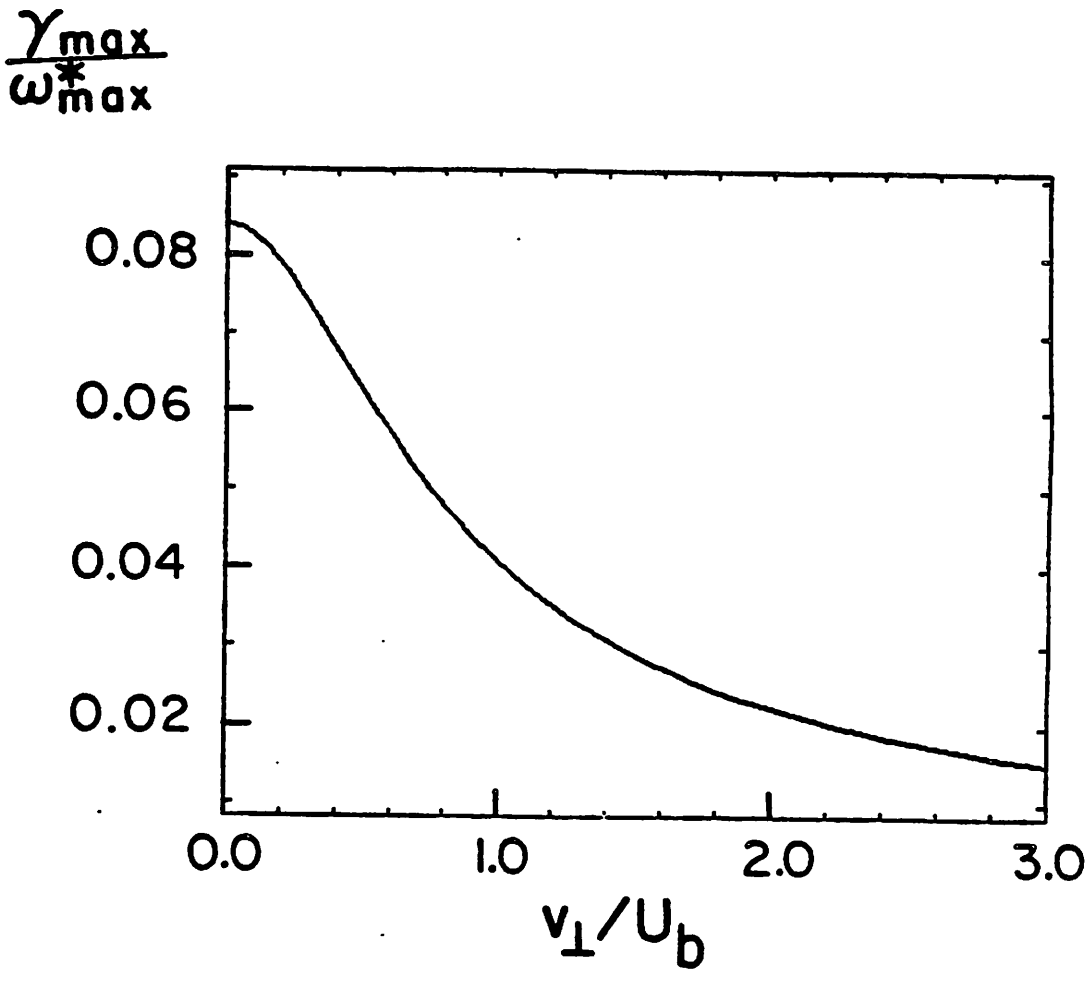

FIG. 4. (a) Normalized maximum growth rate maximized over the k vector as a function of $v_\perp/U_b$ and the corresponding values for (b) the normalized real frequency ω_r/ω_{max}, (c) $k_\perp\rho_s$ and (d) $k_z L_n$.

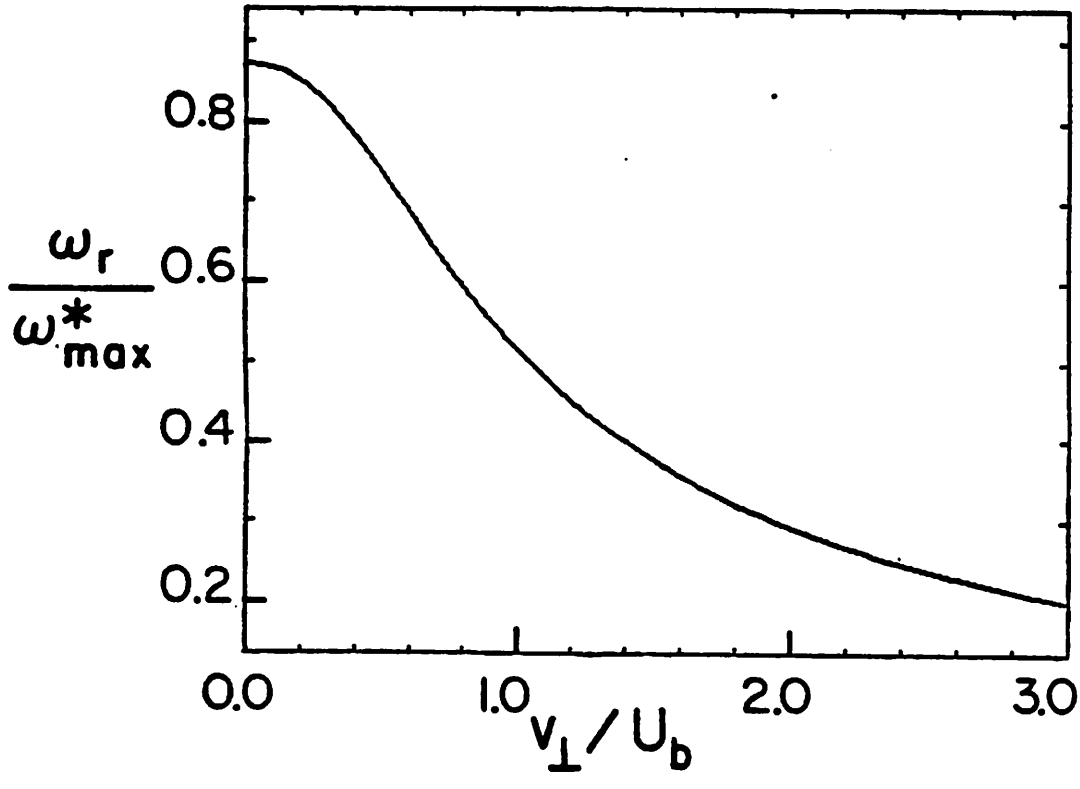

FIG. 4b.

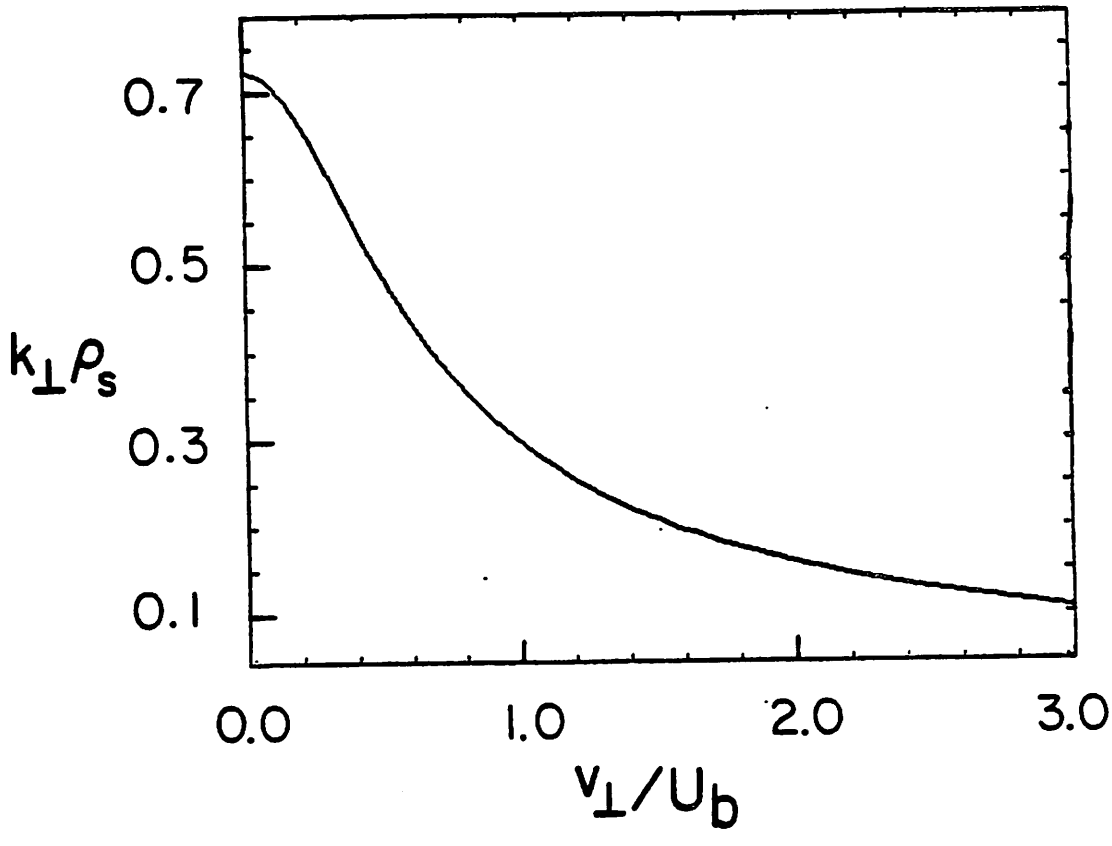

FIG. 4c.

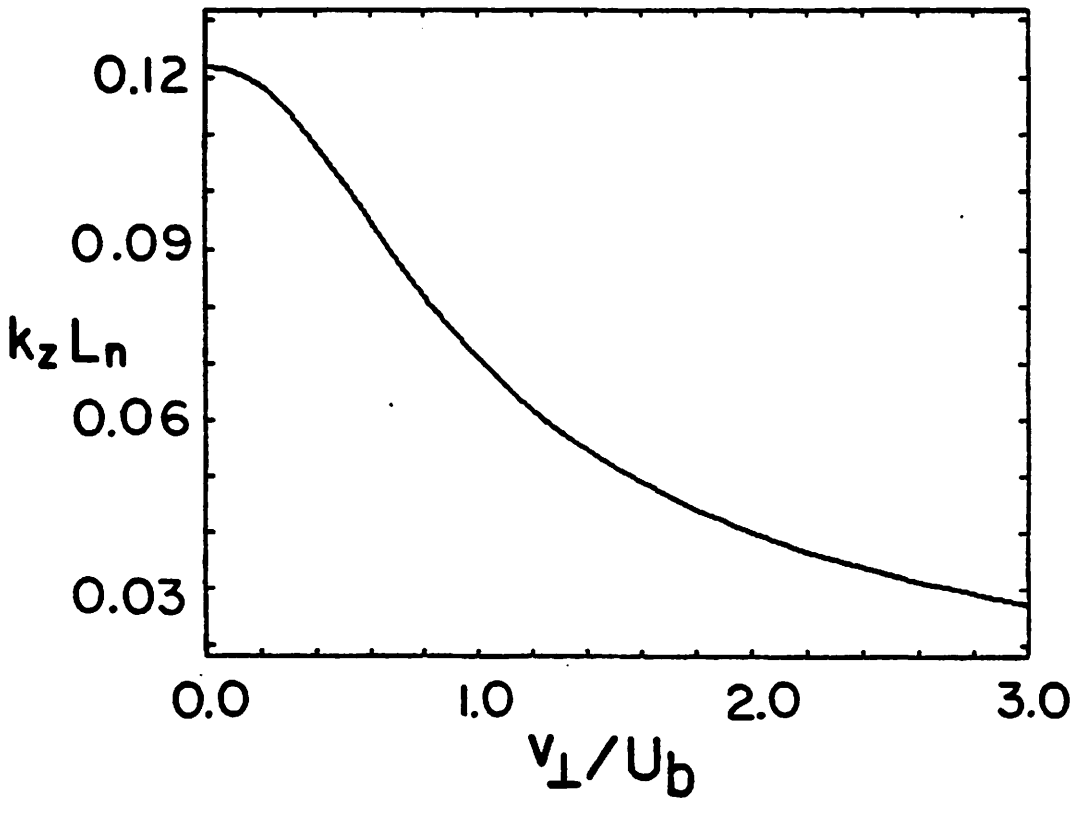

FIG. 4d.

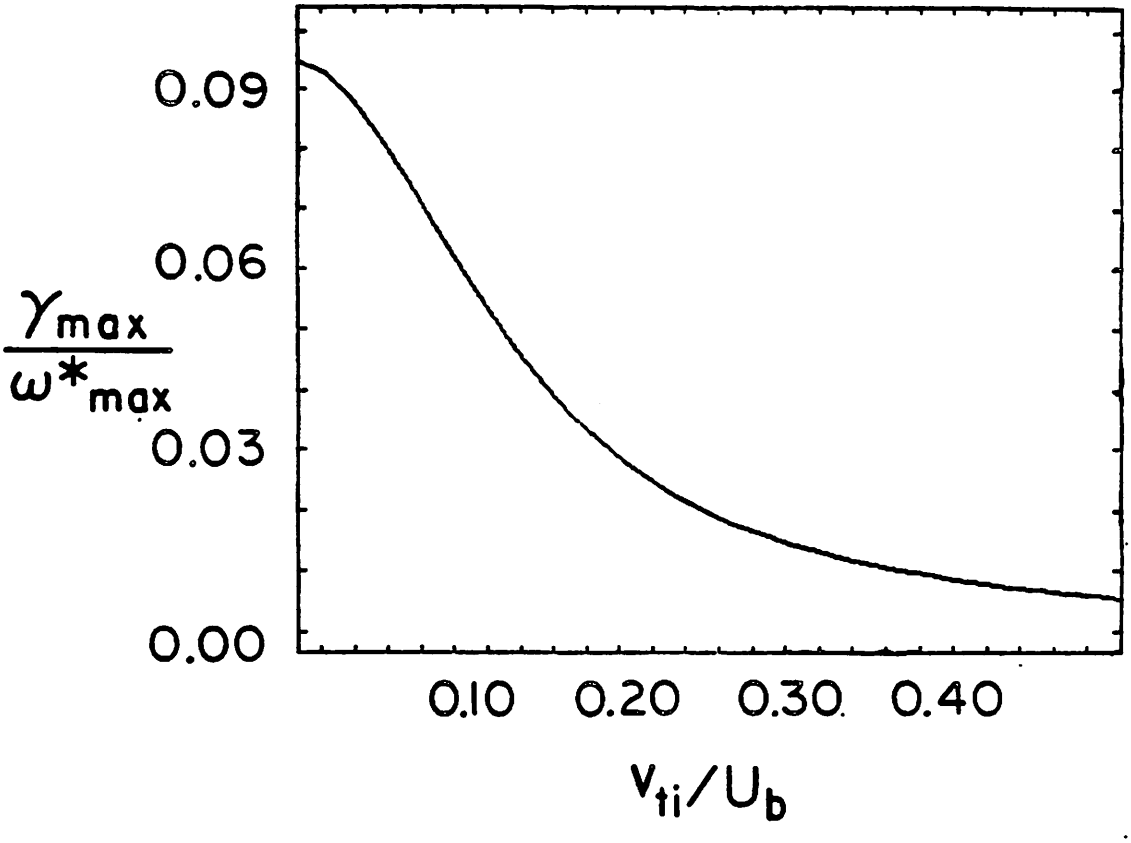

FIG. 5. (a) Normalized maximized growth rate as a function of v_{ti}/U_b and the corresponding values for (b) the normalized real frequency, (c) $k_\perp \rho_s$, and (d) $k_z L_n$.

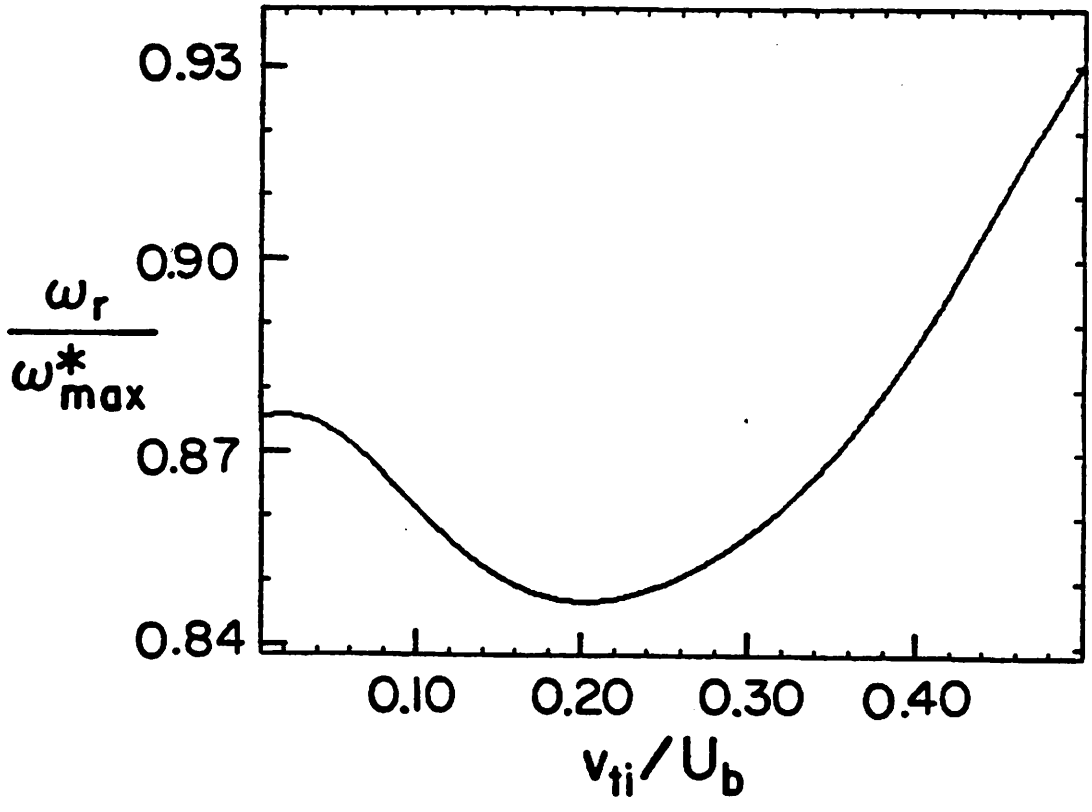

FIG. 5b.

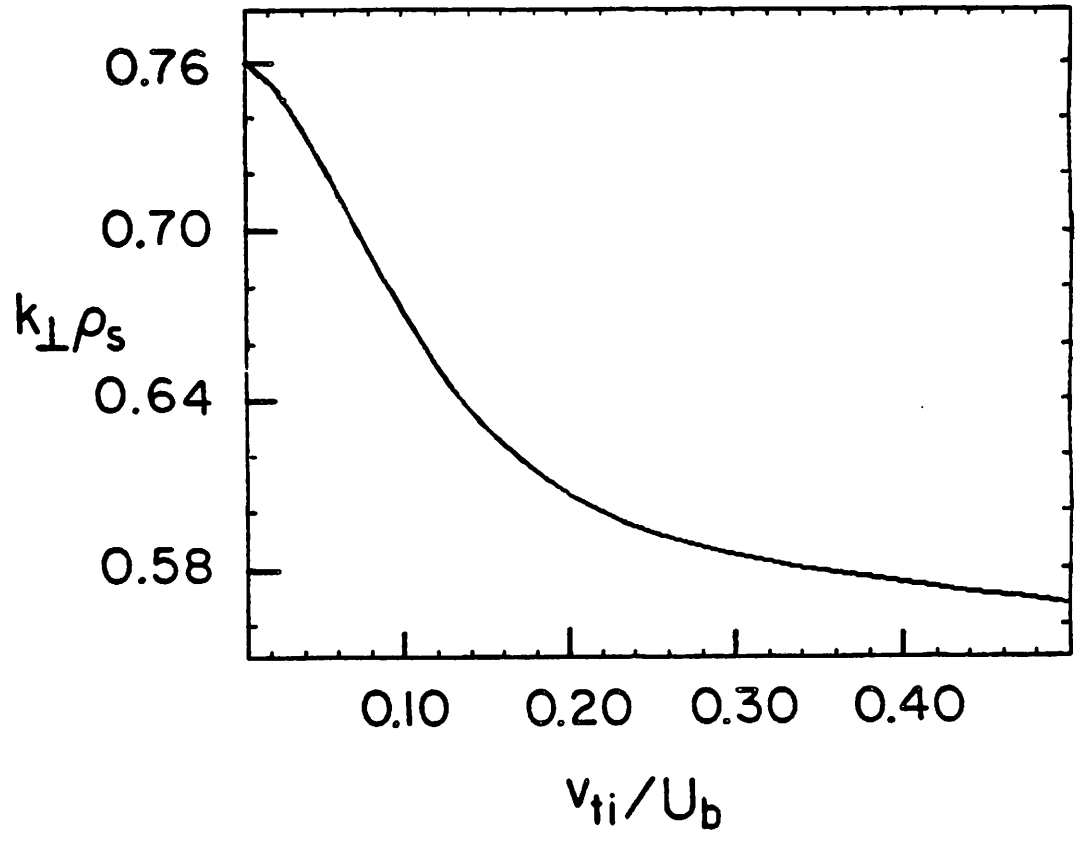

FIG. 5c.

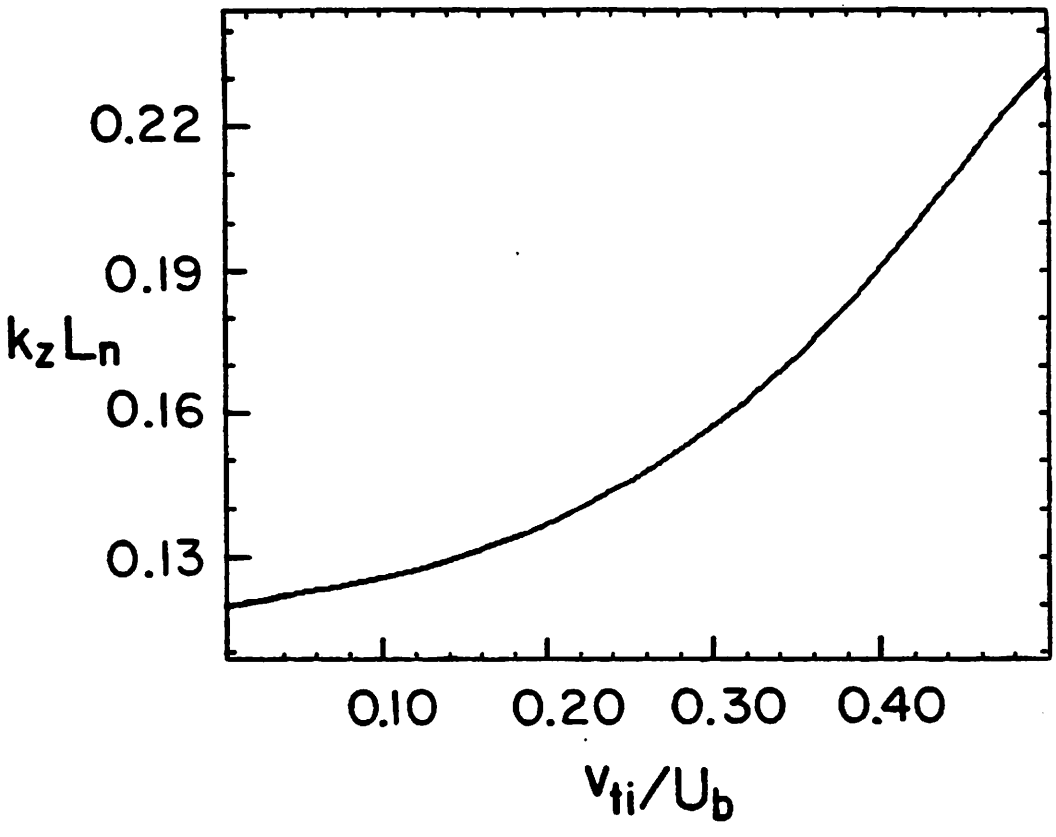

FIG. 5d.

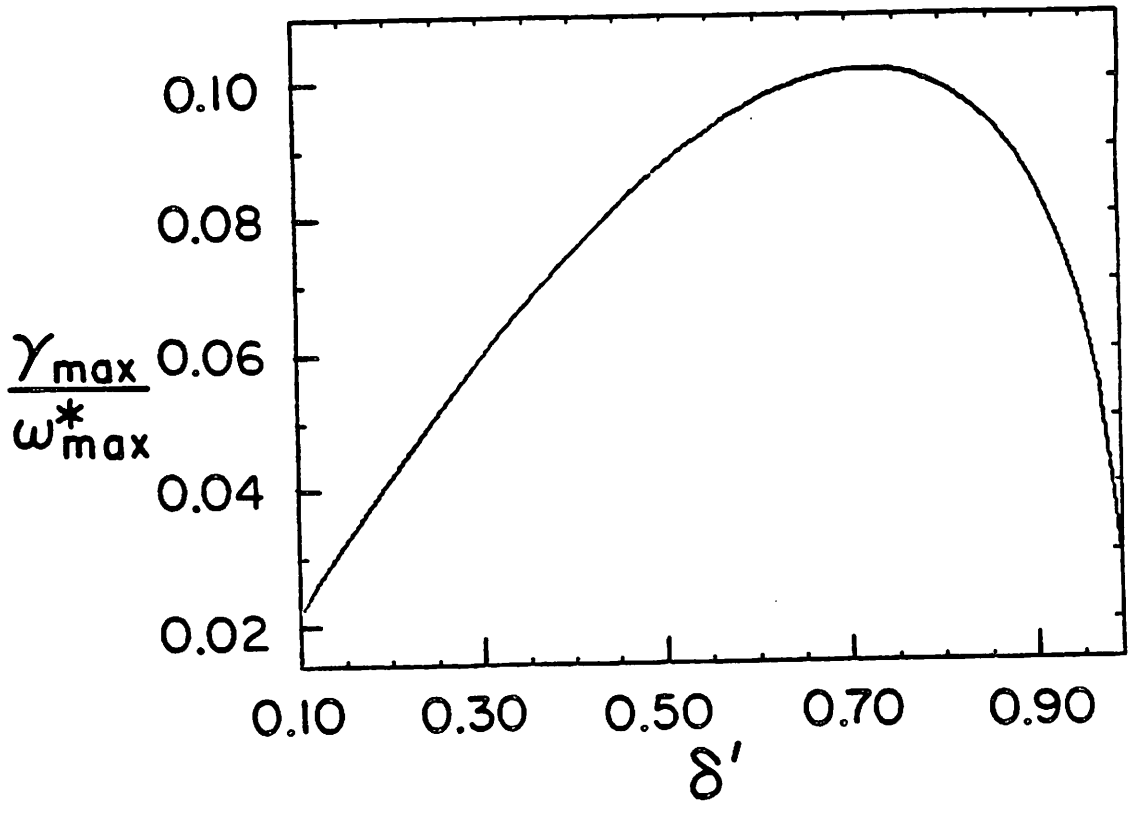

FIG. 6. (a) Normalized maximum growth rate as a function of $\delta' \equiv 1. - \delta$ and the corresponding values of (b) the normalized frequency ,(c) $k_\perp \rho_s$, and (d) $k_z L_n$.

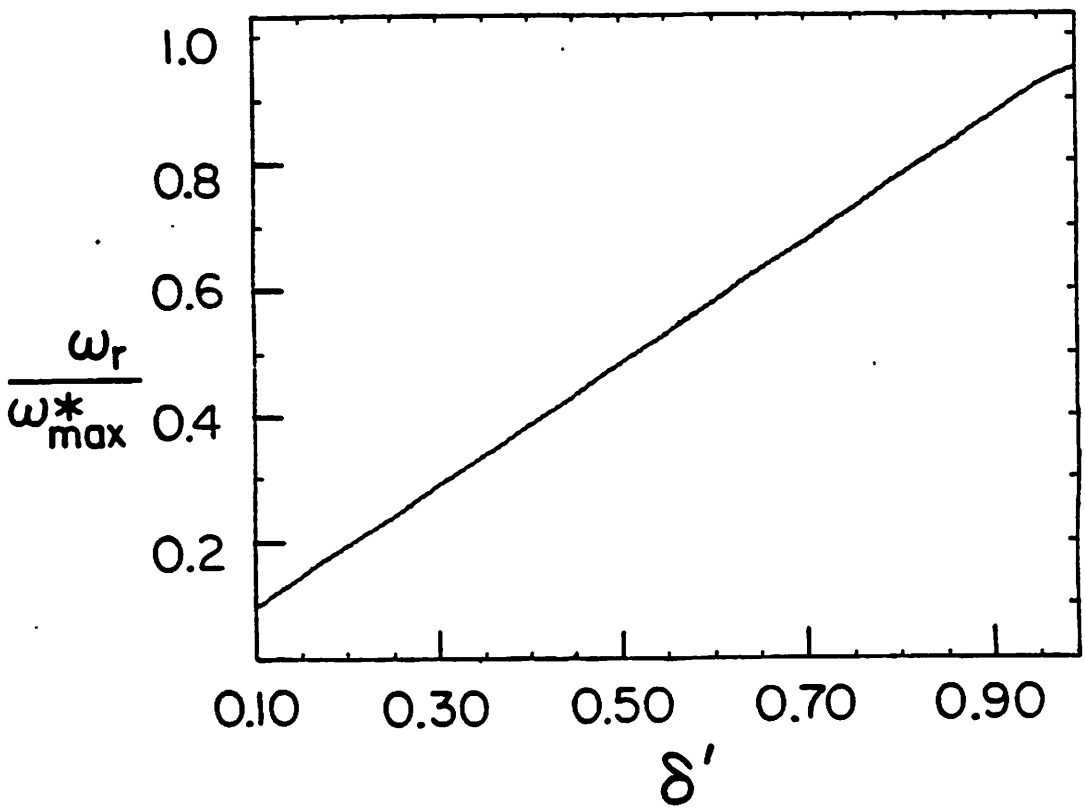

FIG. 6b.

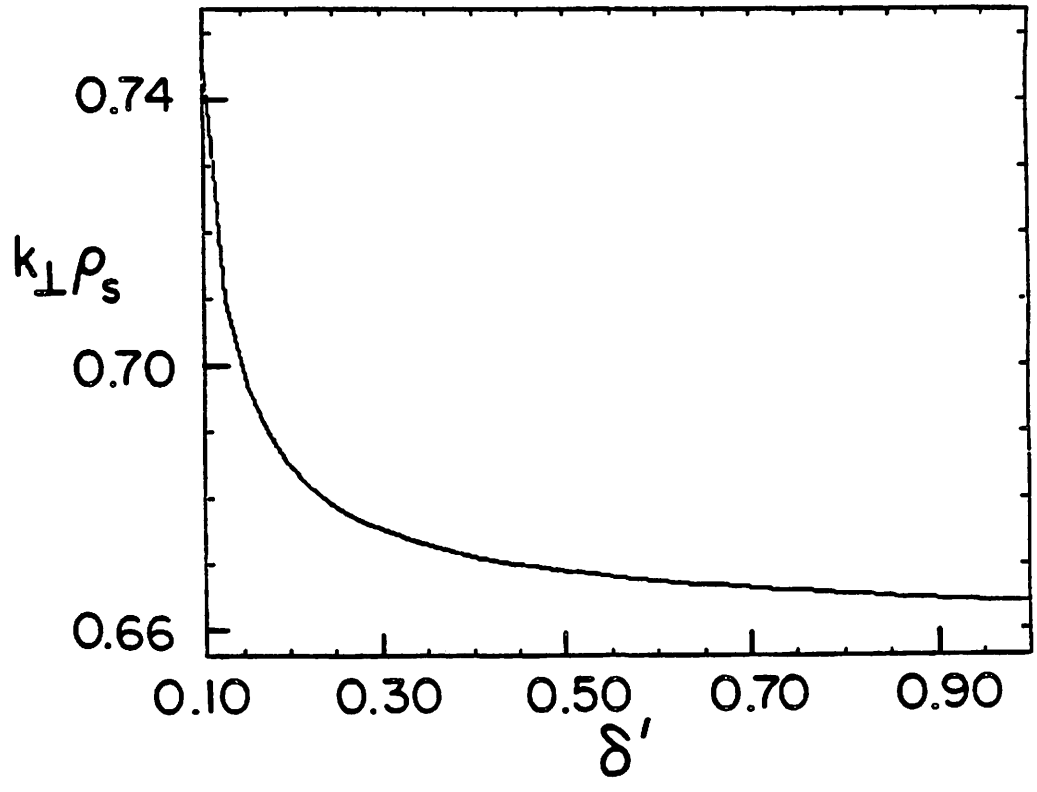

FIG. 6c.

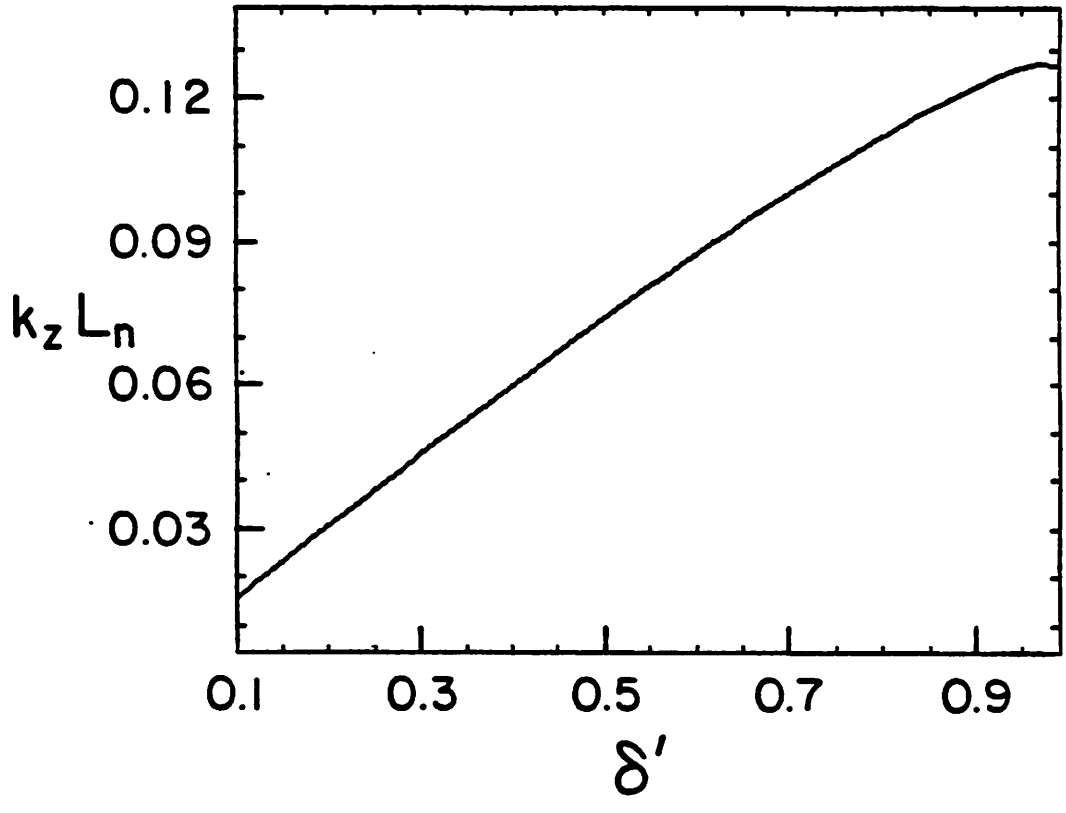

FIG. 6d.

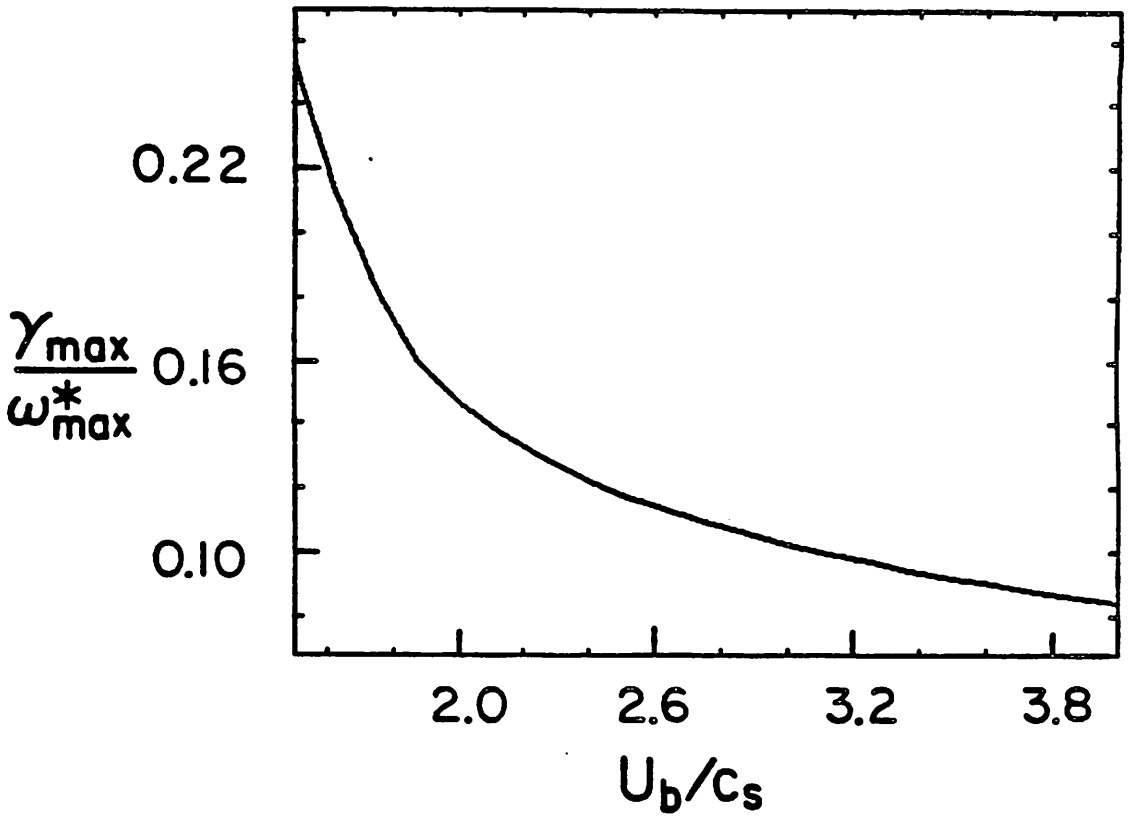

FIG. 7. (a) Normalized maximum growth rate as a function of U_b/c_s and the corresponding values of (b) the normalized real frequency, (c) $\rho_s k_\perp$, and (d) $k_\parallel L_n$.

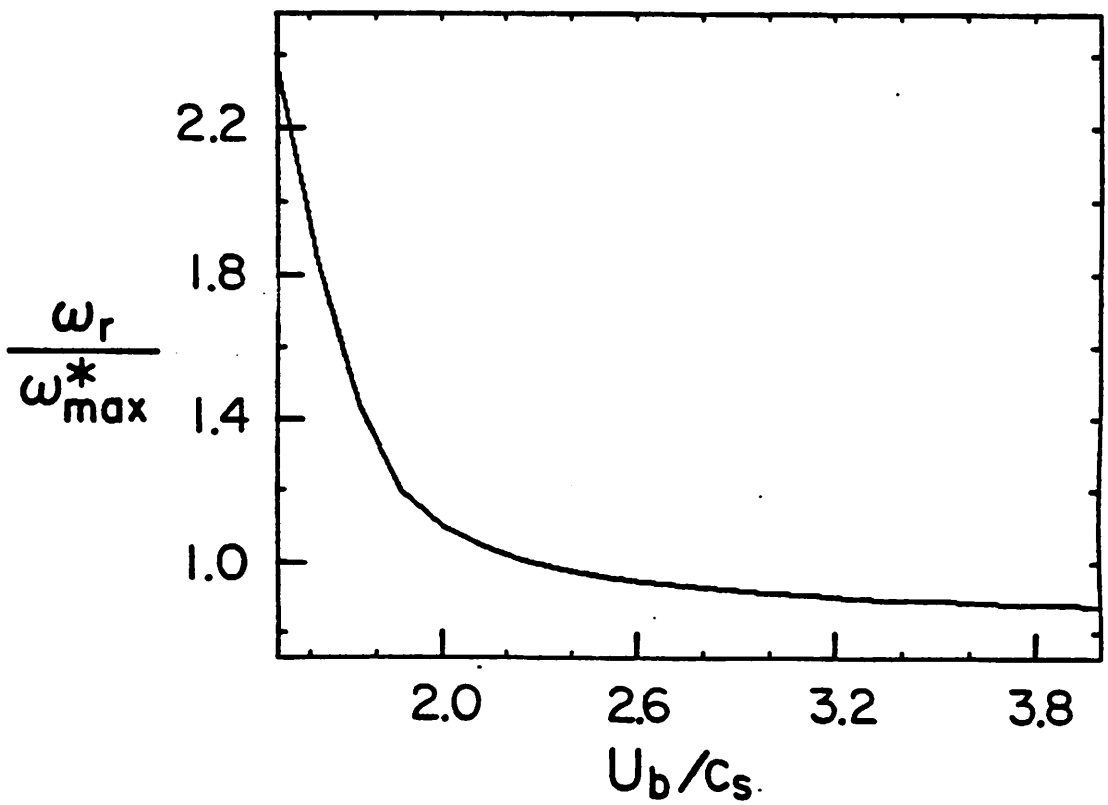

FIG. 7b.

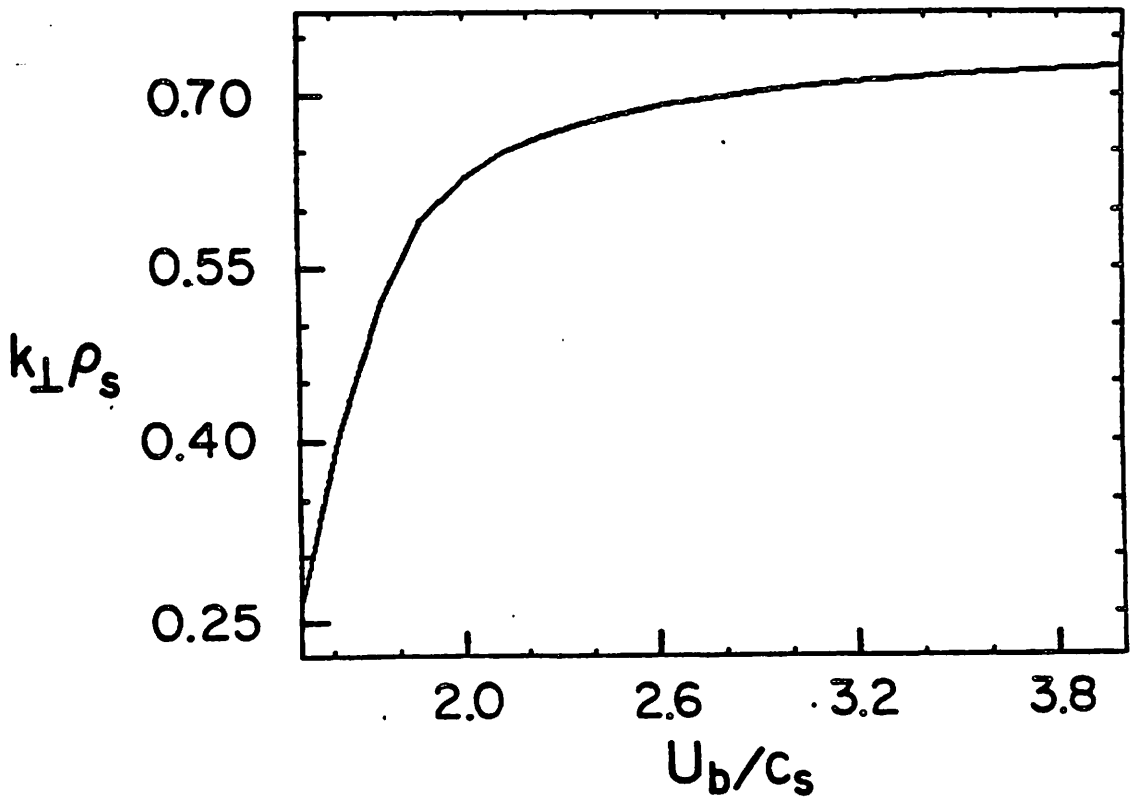

FIG. 7c.

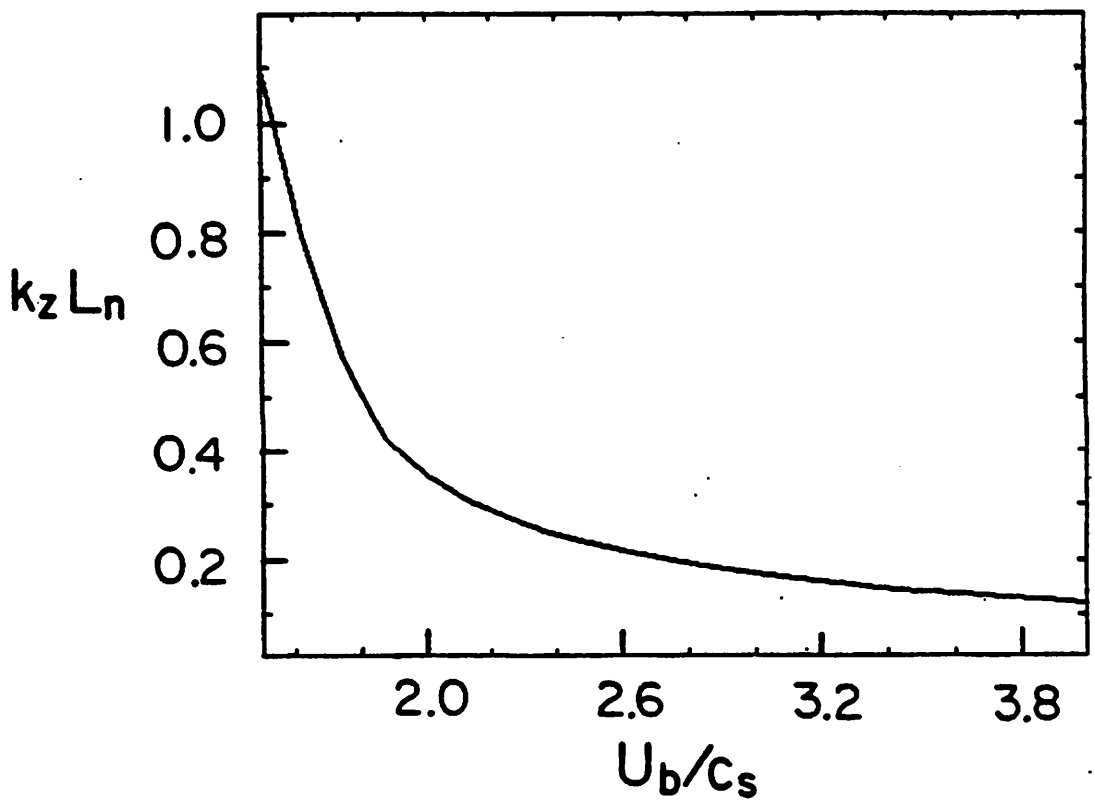

FIG. 7d.

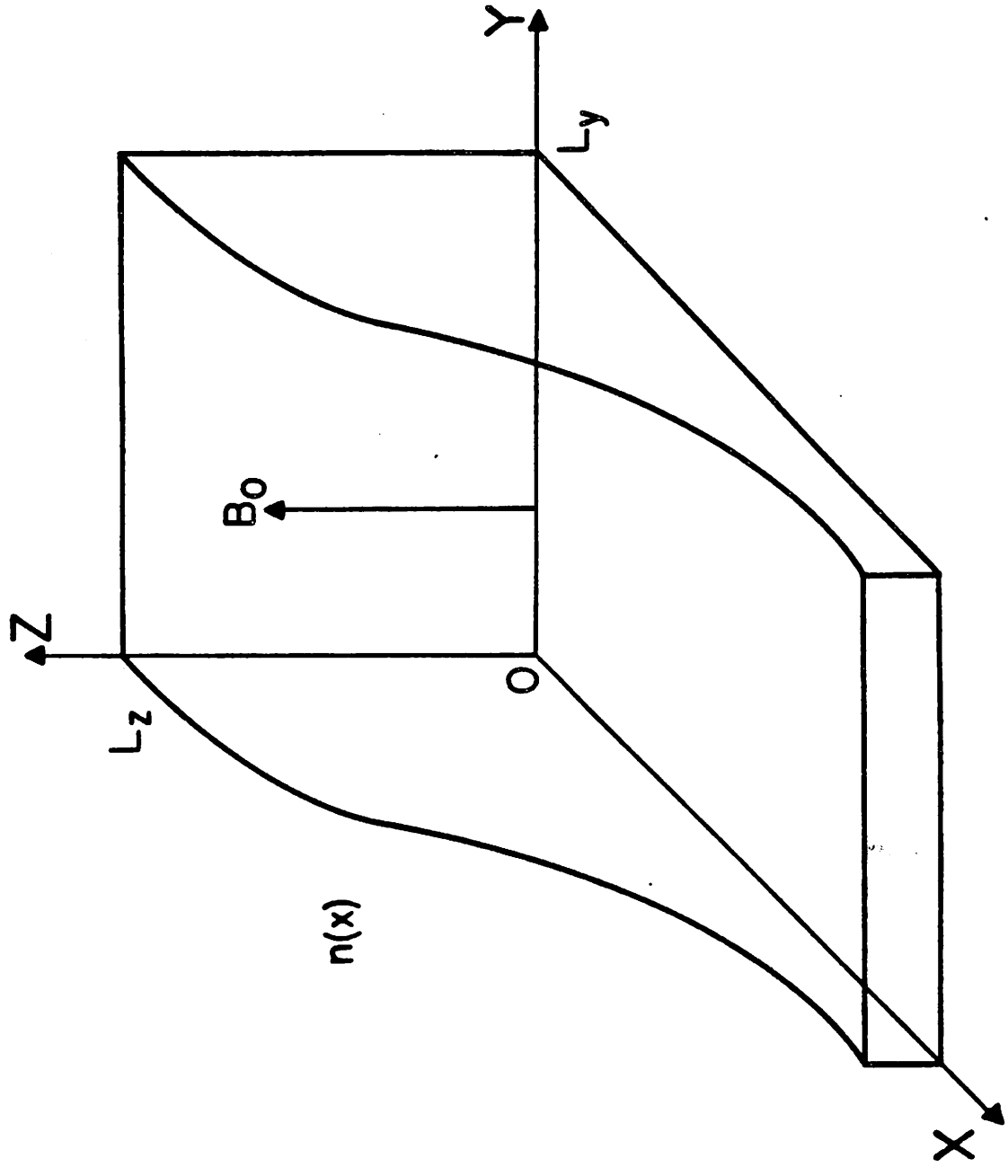

FIG. 8. Simulation geometry. The density is only a function of the x coordinate: B_0 is uniform and entirely in the z direction.

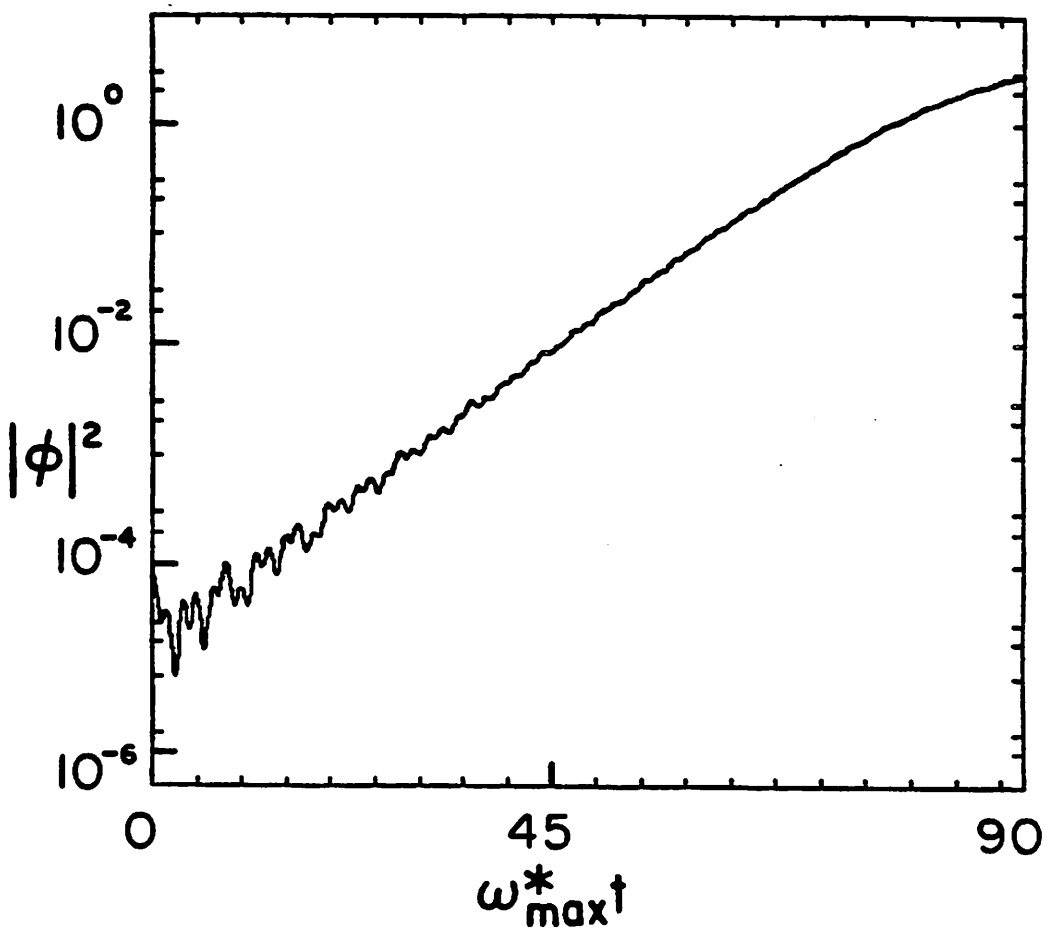

FIG. 9. Time histories of (a) the square of the mode amplitude and (b) the square of the real portion of the potential for a given position in z. For this simulation $v_{\parallel}/U_b = 0.19$. Random excitation was used to initialize the simulation.

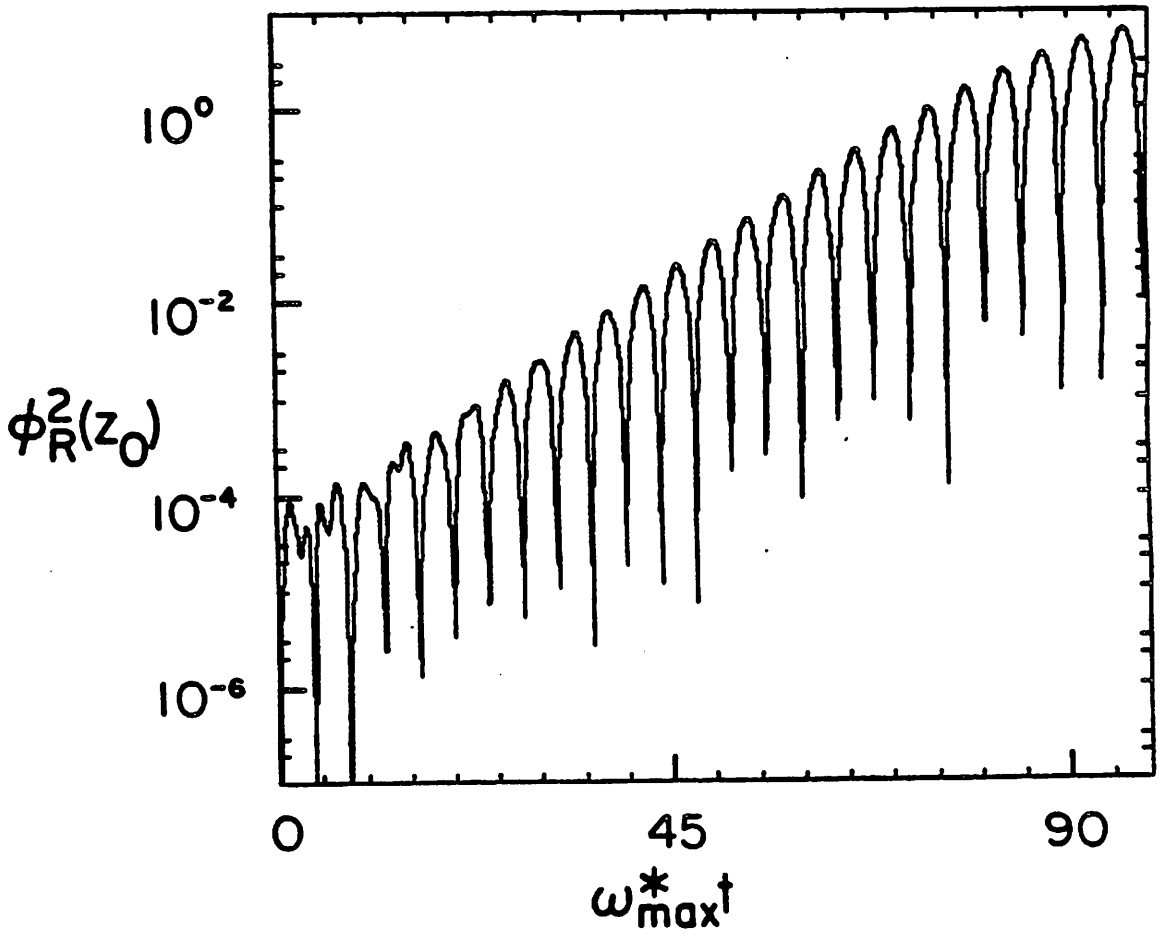

FIG. 9b.

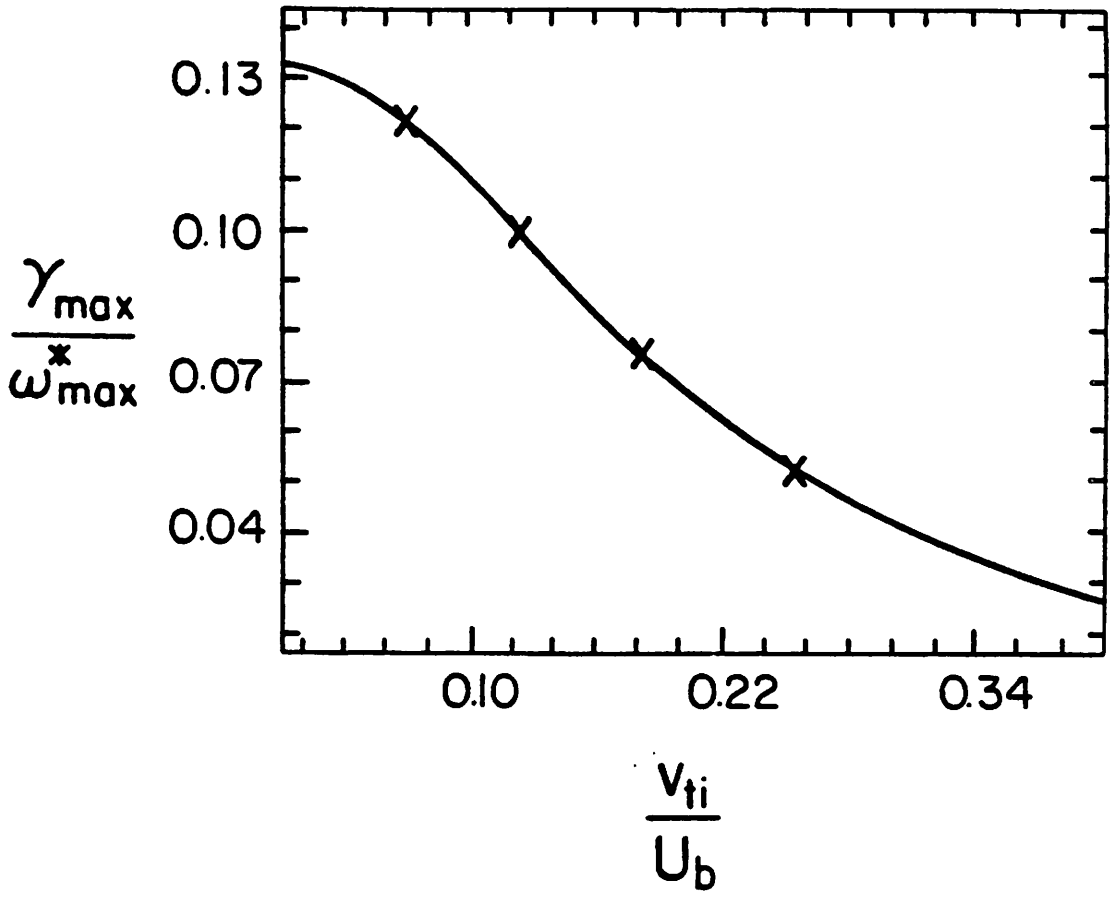

FIG. 10. Theoretical maximum growth rates given by the curve are compared with the simulation results given by the crosses. The approximate error in the measurements is given by the width of the crosses.

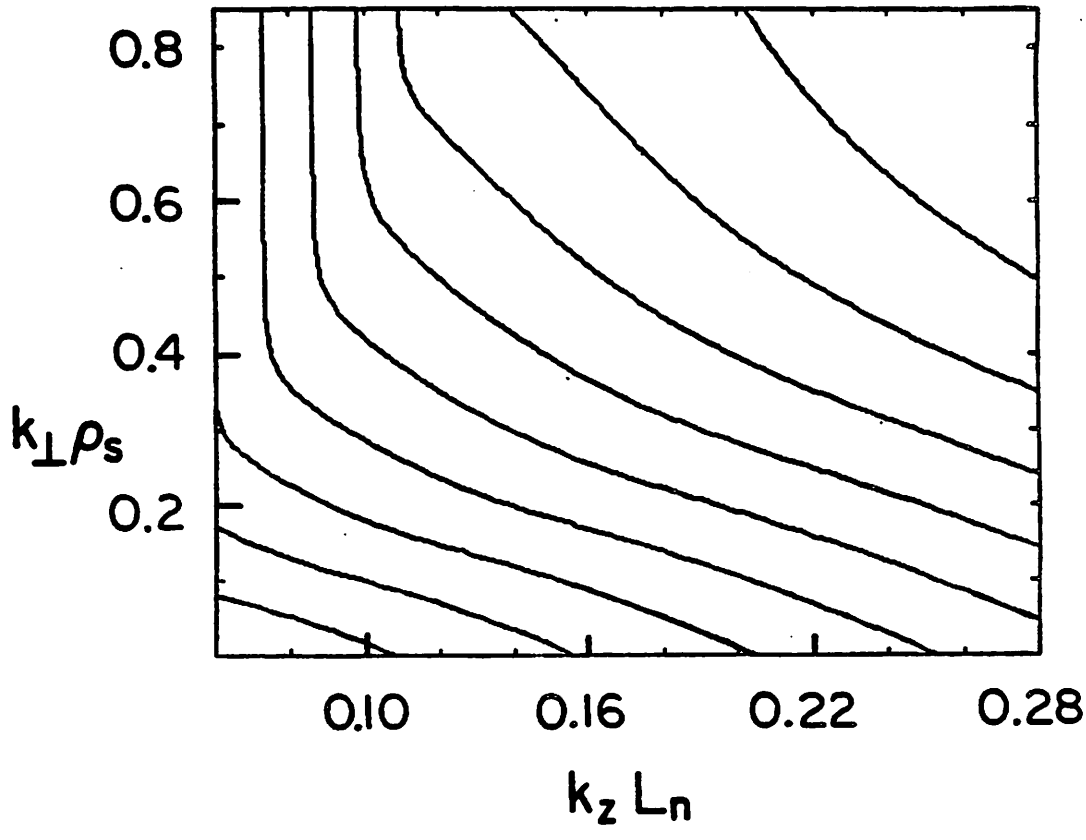

FIG. 11. Variation of (a) the real frequency and (b) the growth rate in the $k_z L_n - k_\perp \rho_s$ plane. The parameters are $\delta = 0.2$, $\left(\nu_\perp\right)_0 / U_b = 0.5$, $\Delta = 0.0$, and $\nu_{ii}/U_b = 0.20$. The contour interval in (a) is 0.883 $\omega^{\cdot}_{max}$ with the maximum of 0.9936 $\omega^{\cdot}_{max}$ occurring to the right; the contour interval in (b) is 0.00552 $\omega^{\cdot}_{max}$ with a maximum of 0.0552 $\omega^{\cdot}_{max}$.

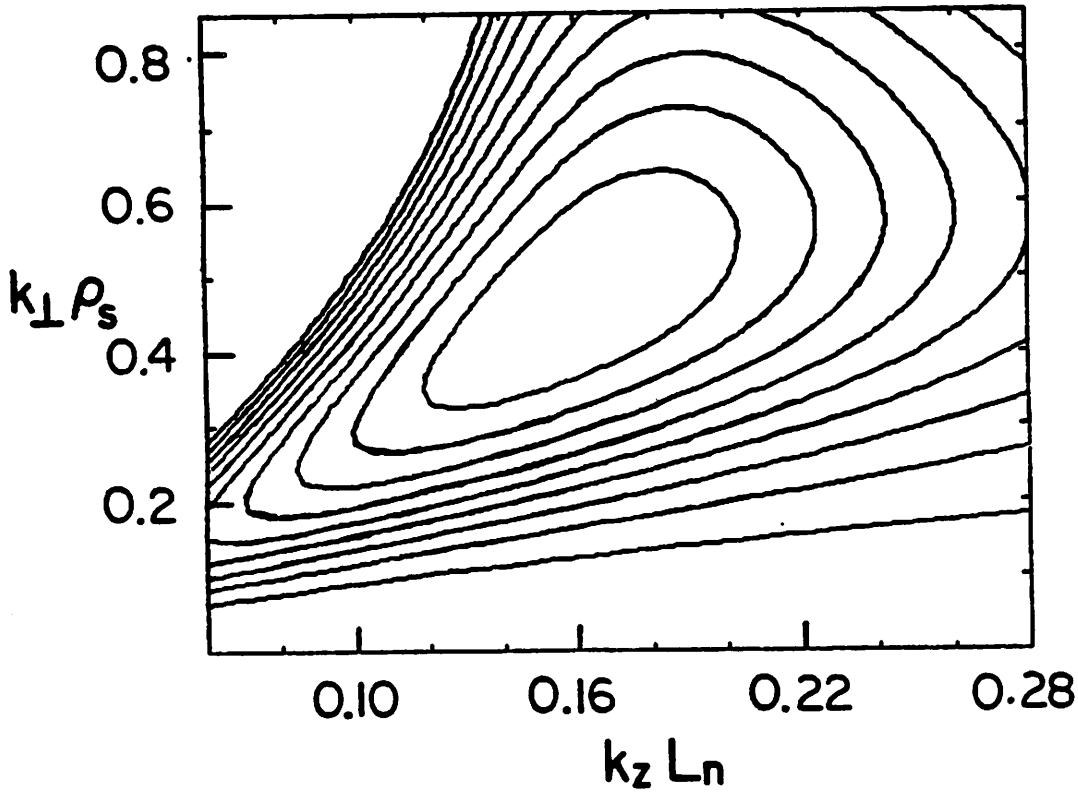

FIG. 11b.

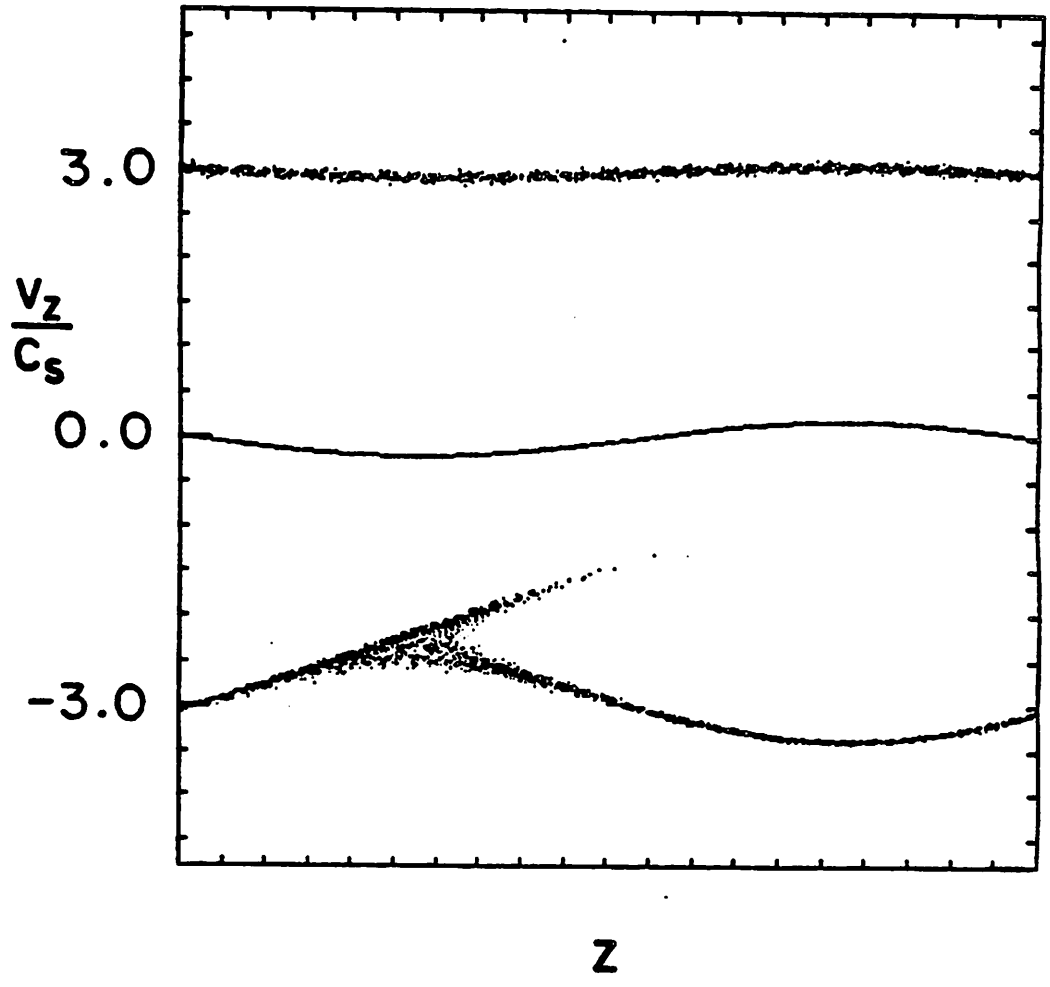

FIG. 12. Particle motion (a) showing both of the ion beams and the background ions in the $z - v_z$ plane and (b) the unstable ion beam in the $z - x/L_n$ plane. Initially all particles are at $x = 0$. Since the background ion density increases with increasing x a positive value for x indicates that the particle has moved in the direction of increasing background ion density. This convention is also used for Fig. 16 and Fig. 19.

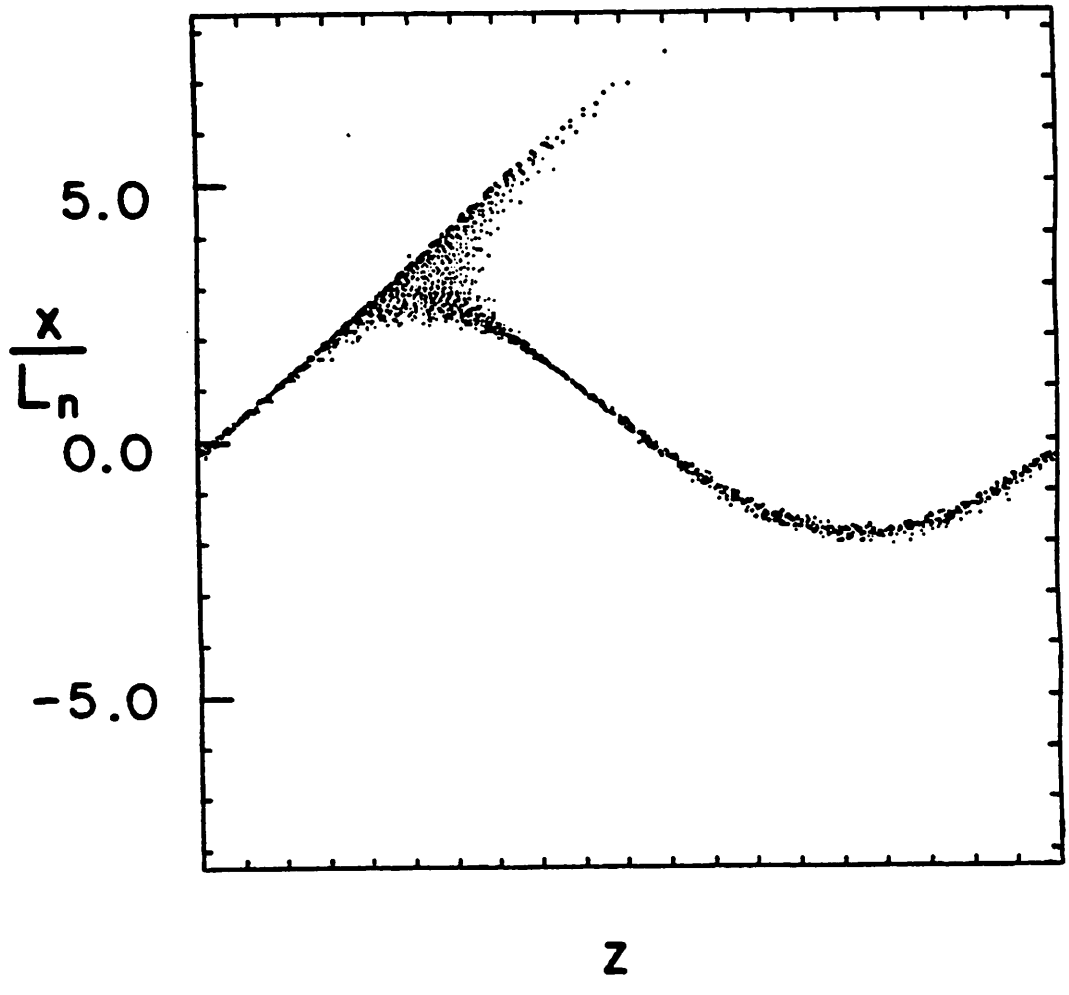

FIG. 12b.

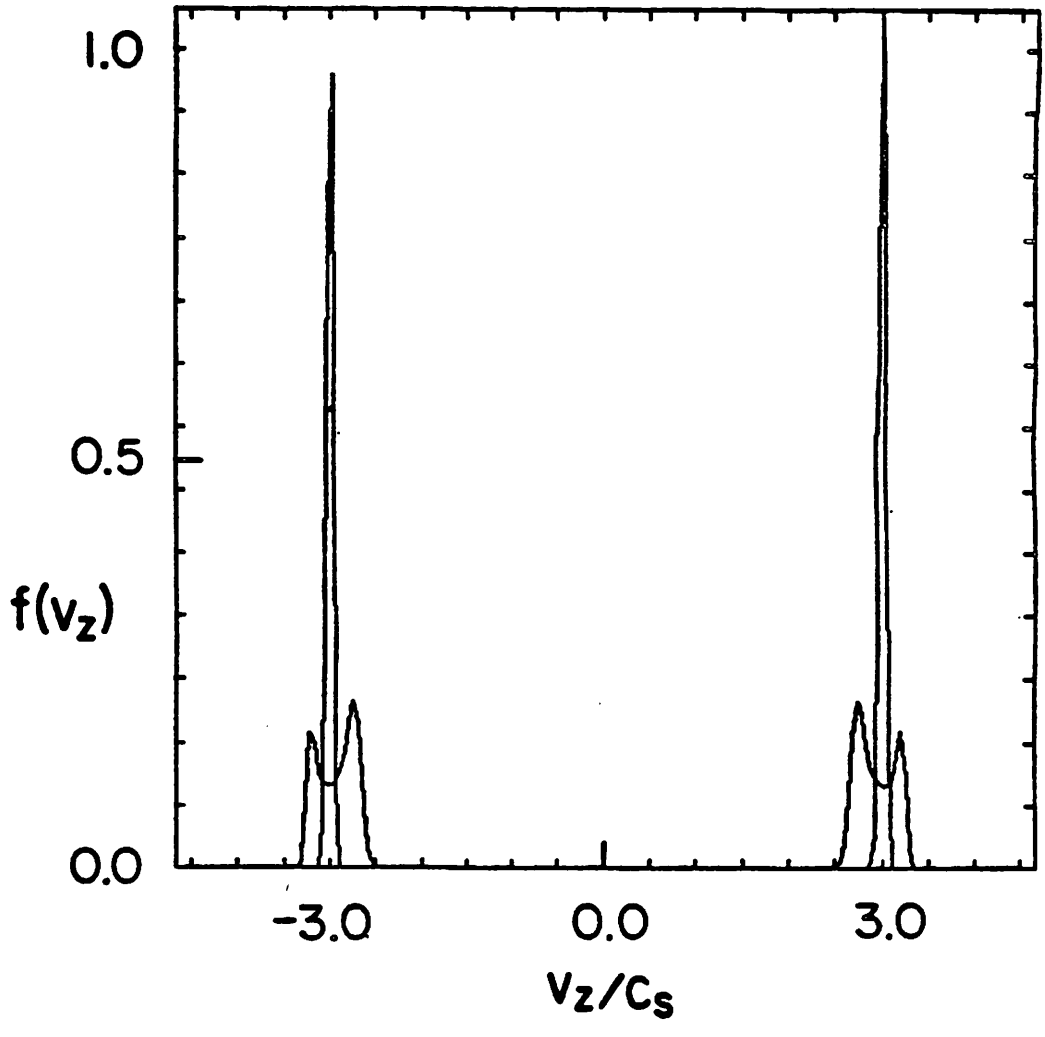

FIG. 13. Ion distribution functions $f(v_z)$ at saturation for the five cases presented in Fig. 10.

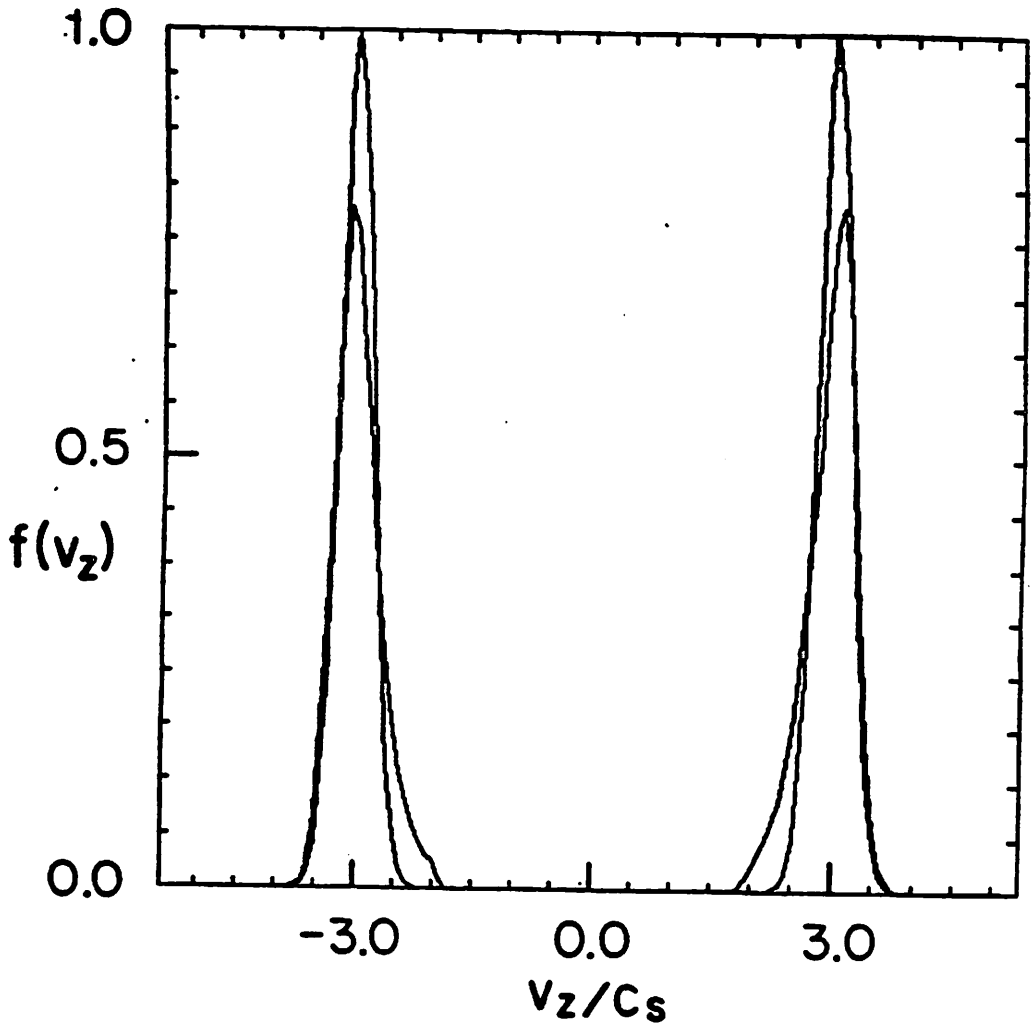

FIG. 13b.

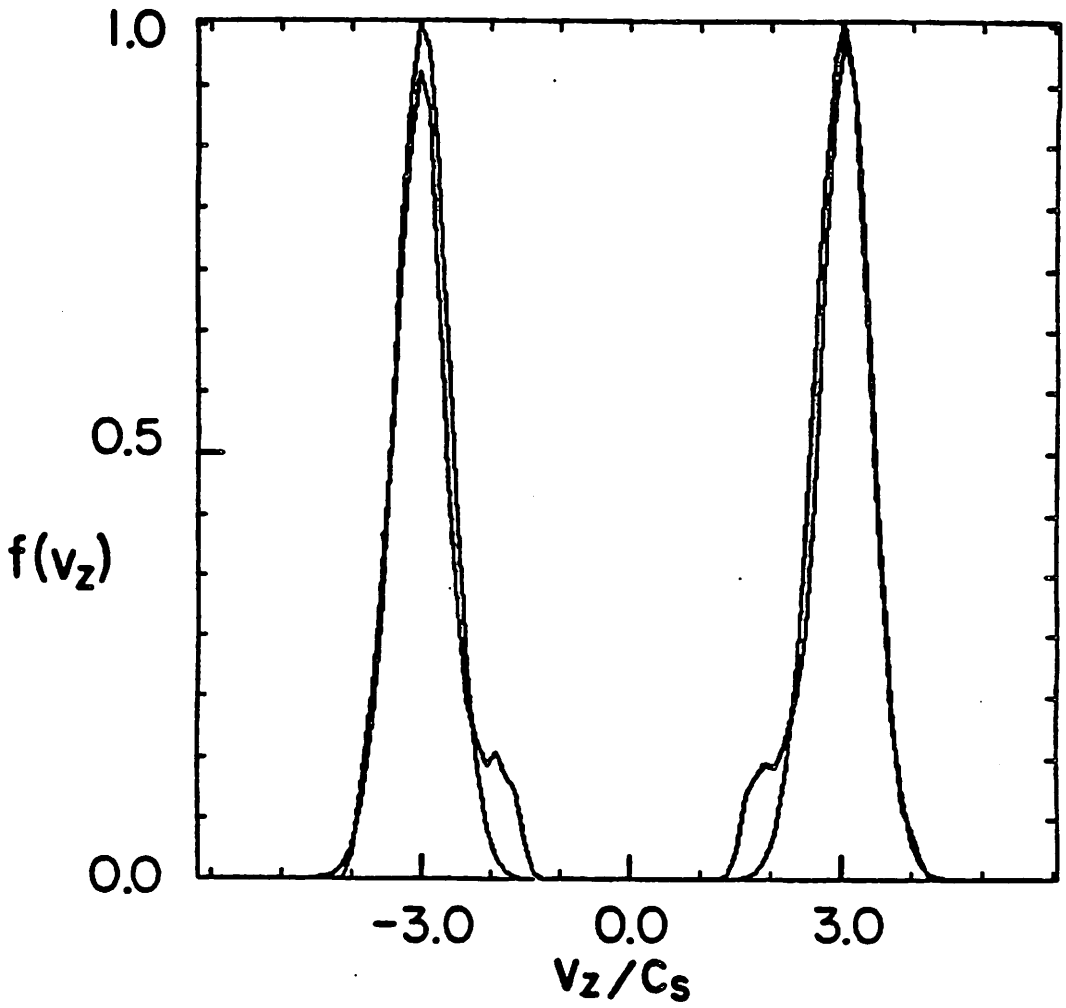

FIG. 13c.

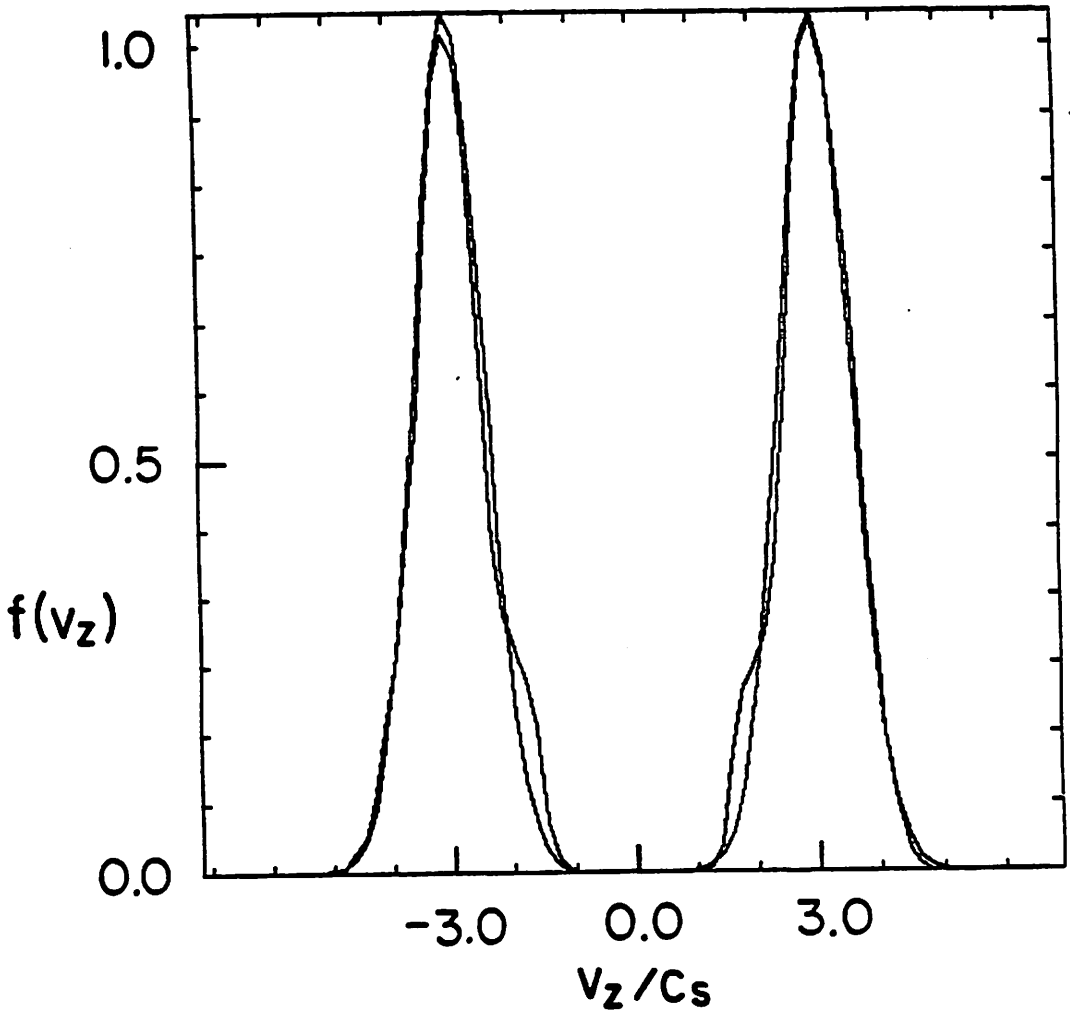

FIG. 13d.

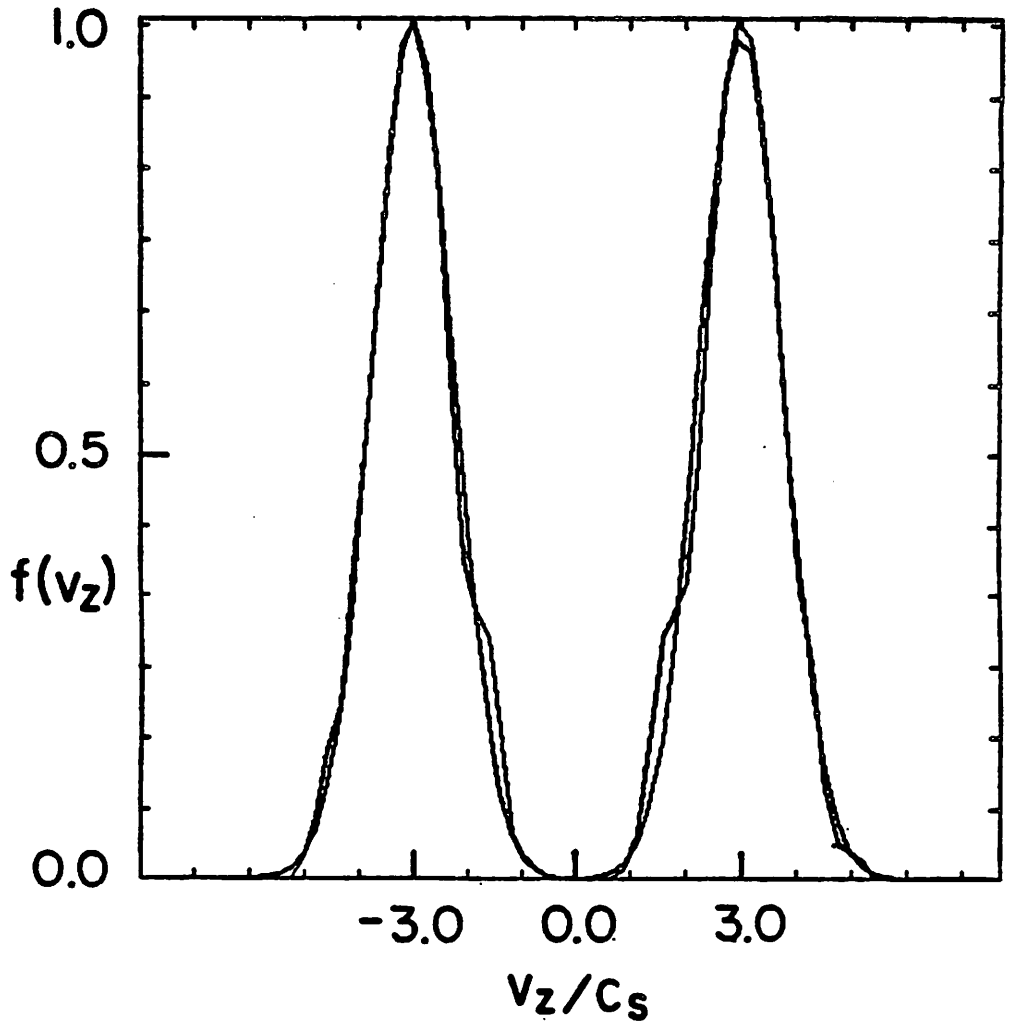

FIG. 13e.

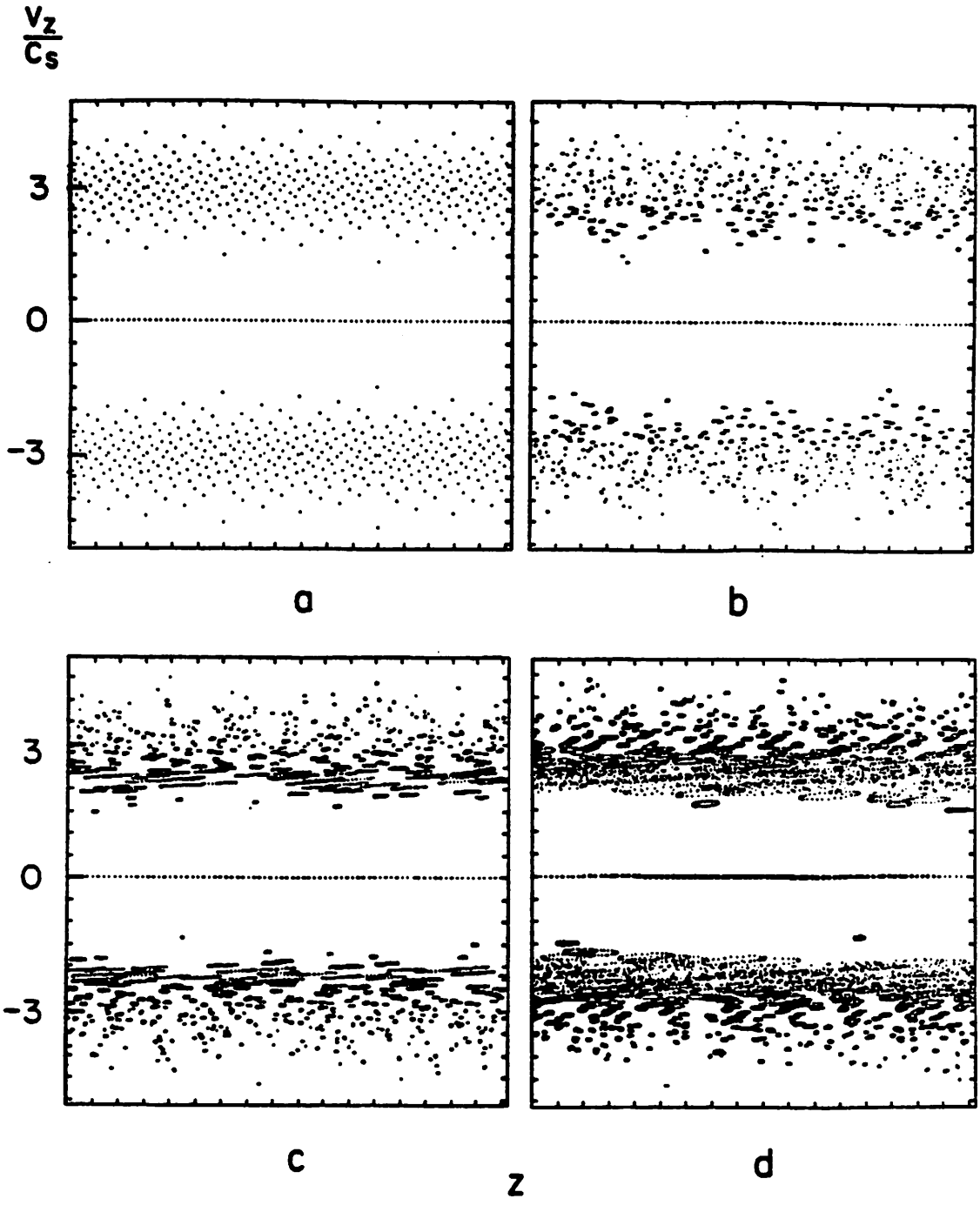

FIG. 14. Ion phase space section $z - v_z$ at (a) $\omega_{max}^{\cdot} t = 0.0$, (b) $\omega_{max}^{\cdot} t = 22.5$, (c) $\omega_{max}^{\cdot} t = 45.0$, (d) $\omega_{max}^{\cdot} t = 67.5$, and (e) $\omega_{max}^{\cdot} t = 90.0$. Initially all particles with the same value of z have the same value of v_z. Particles are loaded uniformly in the y direction. Nonresonant particles execute simple motion whereas the resonant particles suffer large excursions.

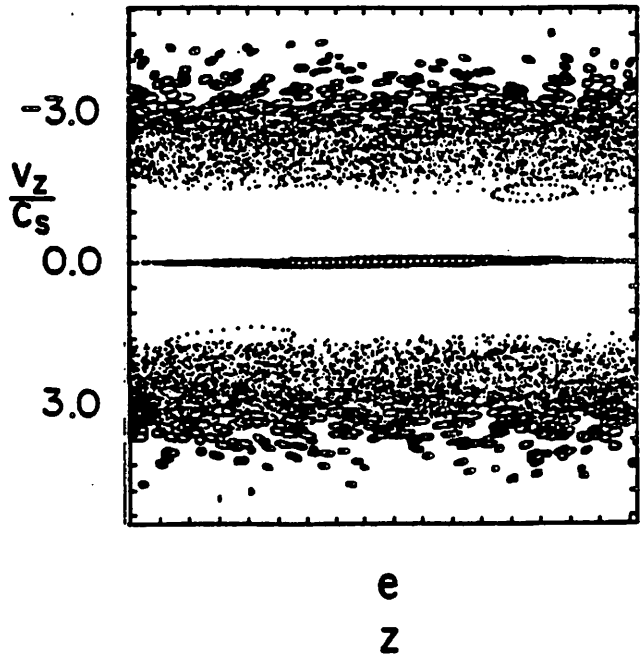
-3.0
$\frac{V_z}{C_s}$
0.0
3.0
e
z

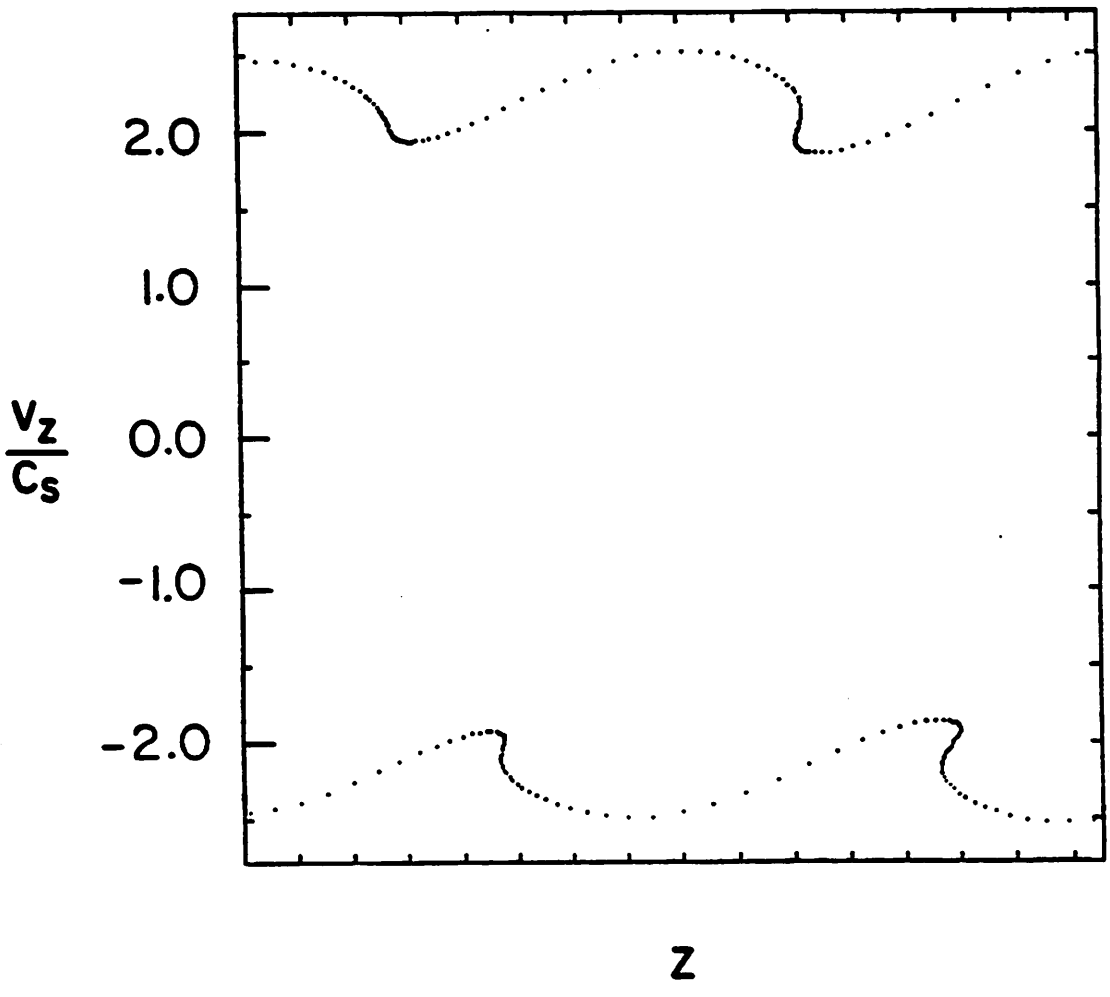

FIG. 15. Test particle phase space for the multimode simulation (a) in the $z - v_z$ plane and (b) in the $z - x/L_n$ plane. Initially, the test particles had a higher speed than the magnitude of the wave phase velocity along the z axis.

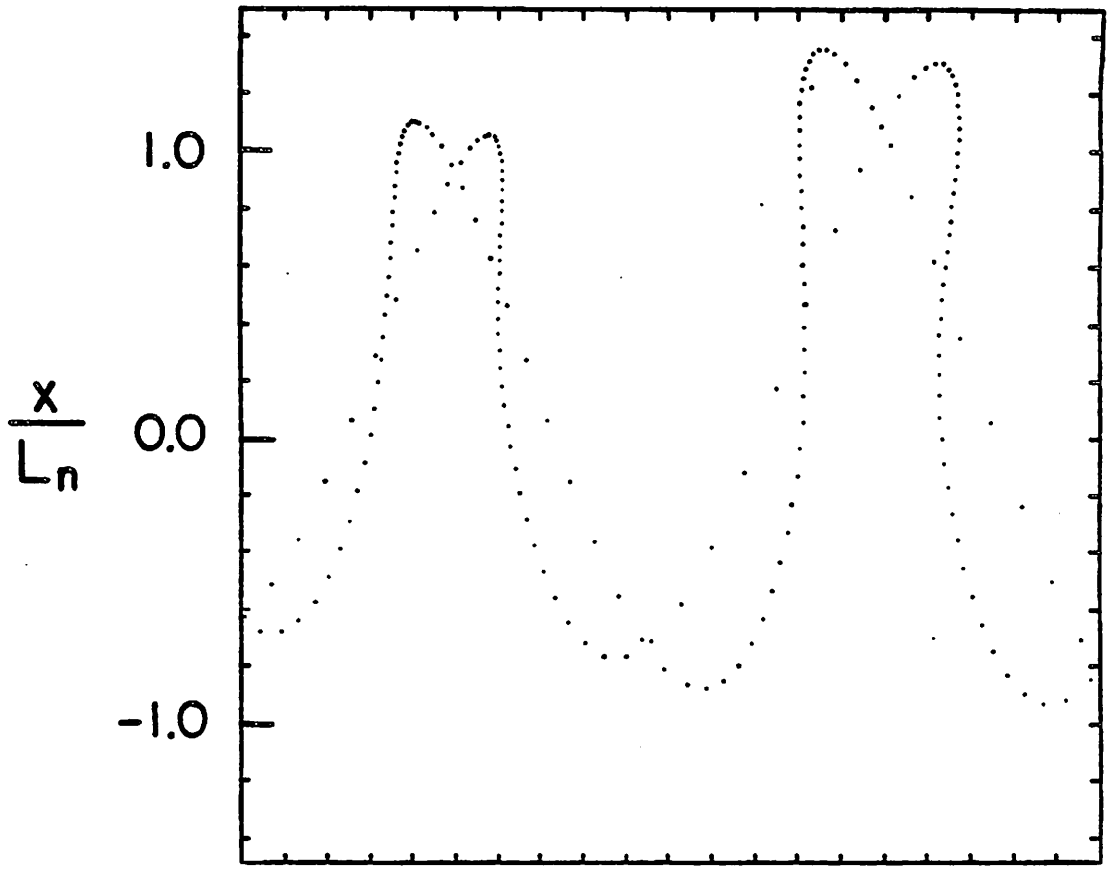

FIG. 15b.

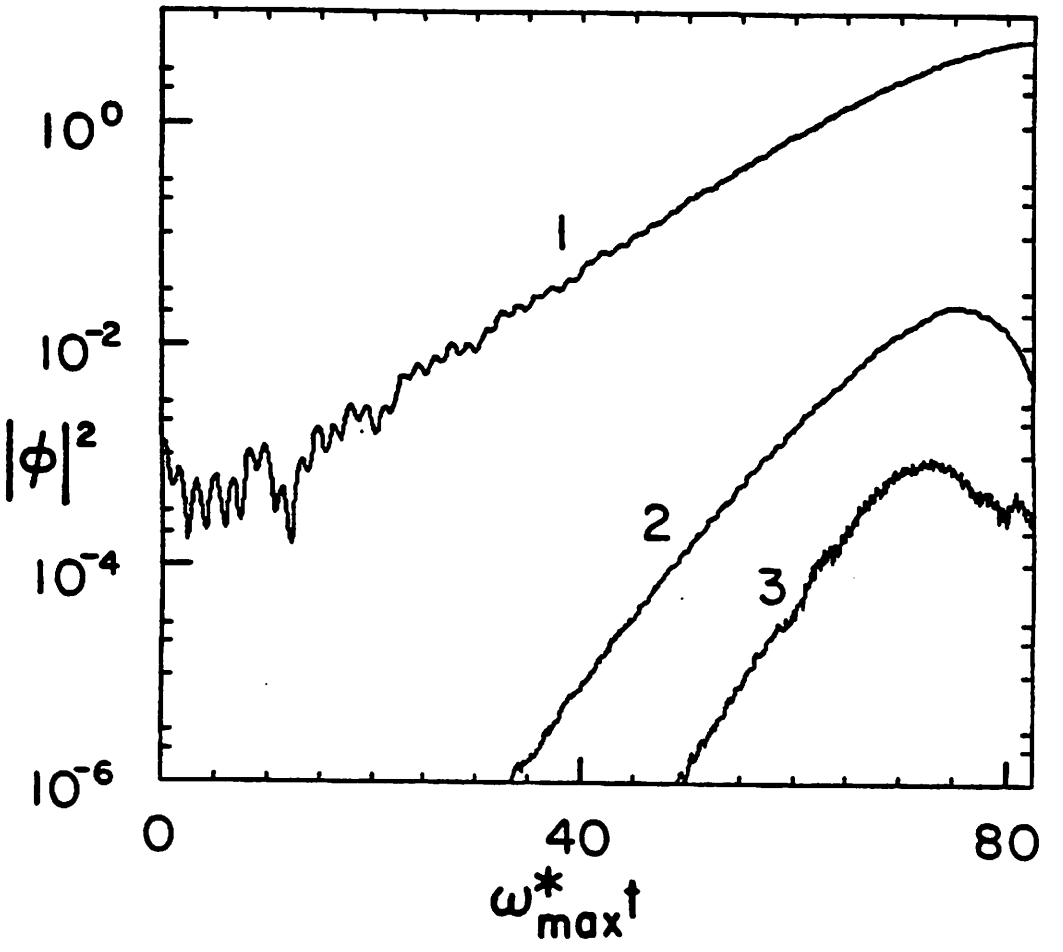

FIG. 16. Mode energies for modes one through three where mode 1 is the only linearly unstable mode. The other modes are multiples of this unstable fundamental mode and have finite amplitude due to mode-coupling. The simulation parameters are $v_n/U_b = 0.0$, $\delta = 0.01$, $U_b/c_s = 3.0$, $\Omega_{ci}\Delta t = 0.40$, 4096 particles for each beam and the background, and there are 65 grids in the y direction and 33 grids in the z direction. Only three Fourier components of the potential were self consistently retained in each direction.

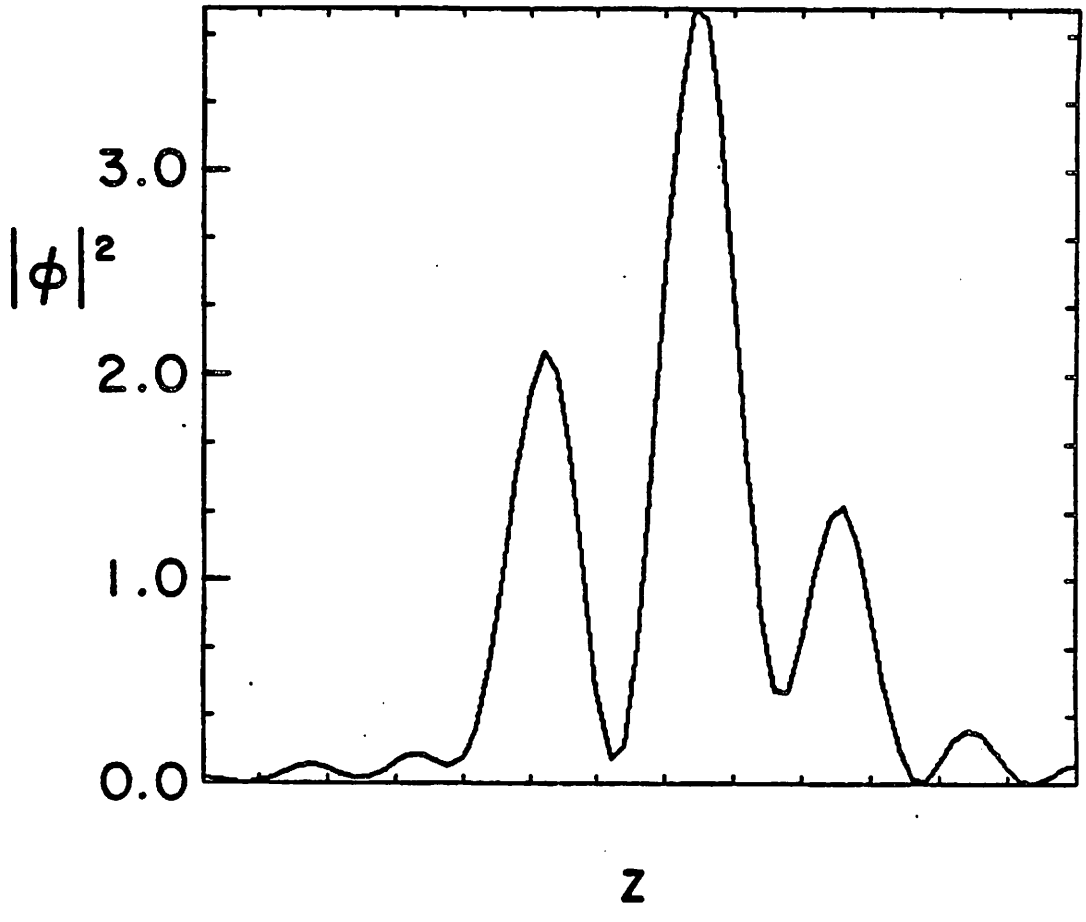

FIG. 17. Magnitude of the potential squared as a function of distance along the magnetic field for a time where the instability is still linear.

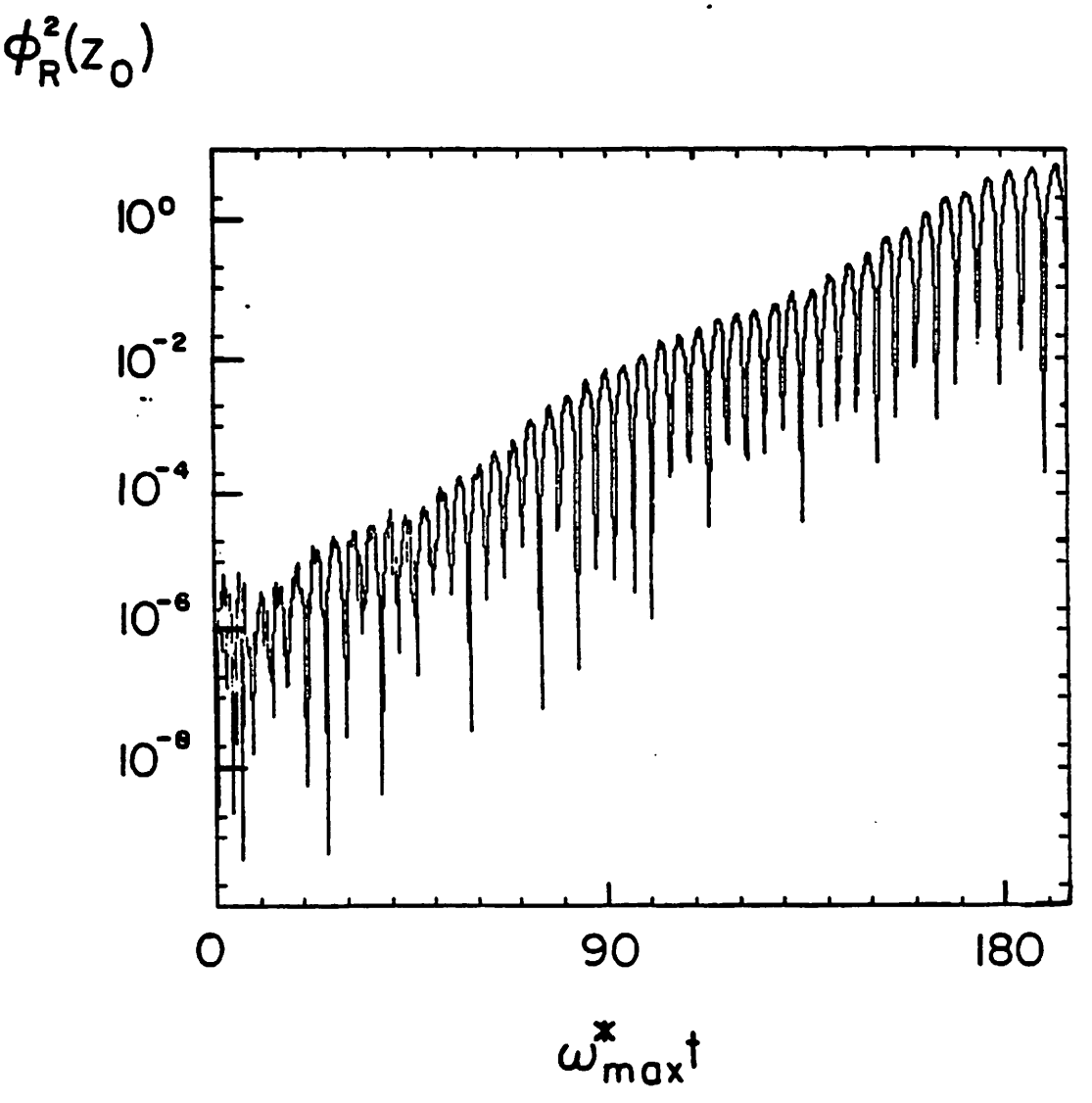

FIG. 18. Square of the real portion of the potential near the center of the simulation region as a function of time.

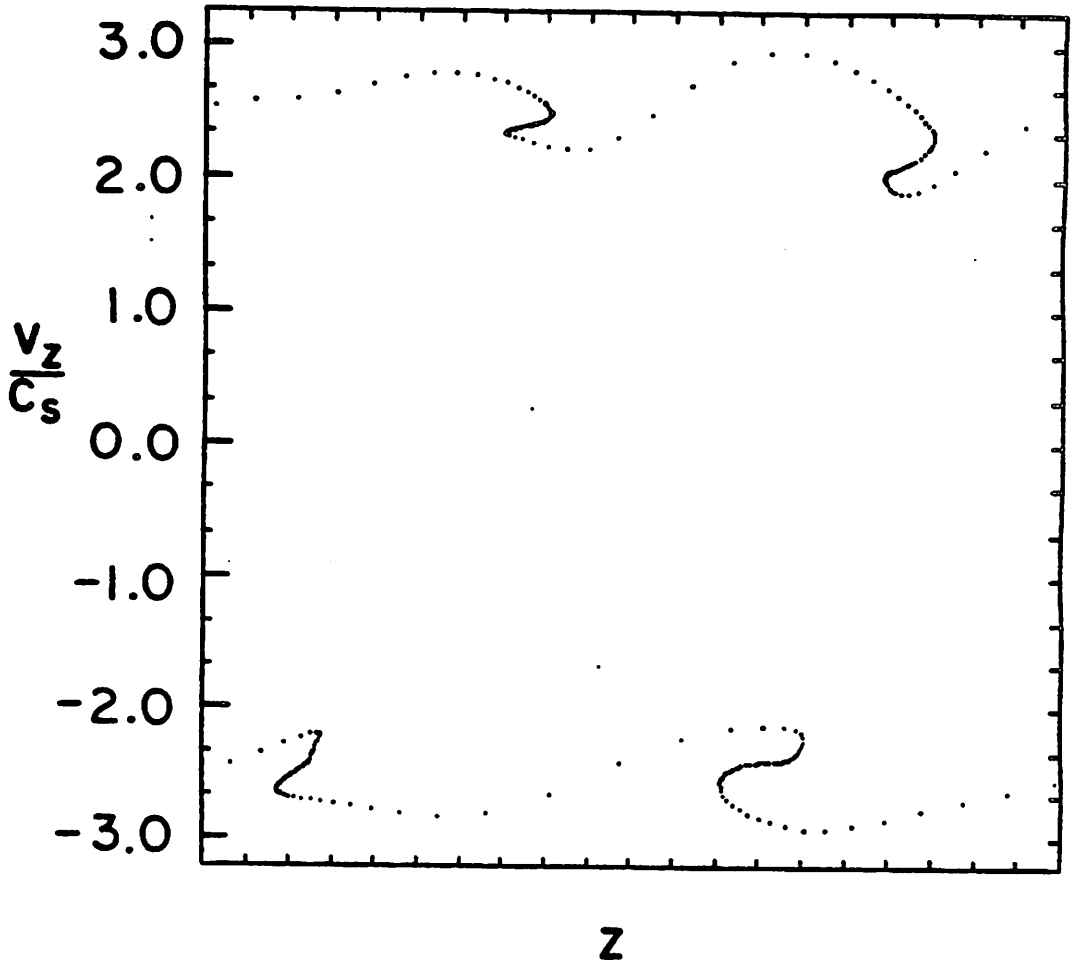

FIG. 19. Test particle trajectories for the axially inhomogeneous simulation; (a) in the $z - v_z$ plane and (b) in the $z - x/L_n$ plane. The test particles were loaded with a higher speed than the wave phase velocity along the z axis.

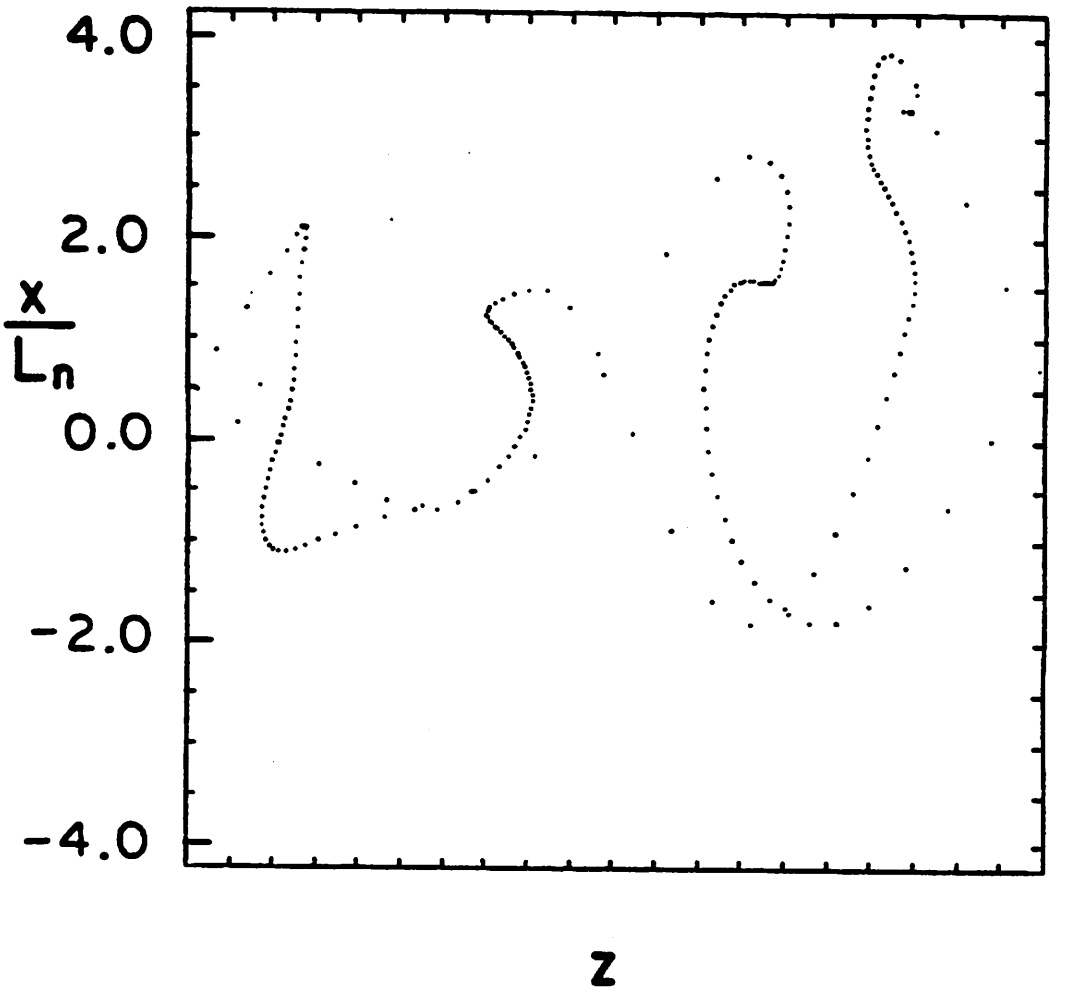

FIG. 19b.